Three-particle correlations with respect to strangeness in pp collisions

Author :

Adrien Vernanchet

Supervisor :

Alice Ohlson

LUND UNIVERSITY

May 2026

Department of Physics, Division of Particle and Nuclear Physics

Thesis submitted for the Master degree in Particle Physics, FYSM64

Abstract

High-energy proton-proton collisions such as the ones happening at the LHC can result in the formation of the QGP, a state of matter similar to the early Universe's. One property of the QGP is strangeness enhancement, leading to the formation of strange flavoured particles such as Ξ, Λ or K. The aim of this thesis is to study the production mechanism of a strangeness-balanced triplet ($\Xi^- K^+ K^+$) through its angular correlation functions and balance function. This is done through the use of Monte-Carlo generated data using the PYTHIA software, as well as real data from the CERN ALICE experiment. Data is then analysed using the ROOT framework in both cases. Final results provide us with a negative ridge along the values where the difference in azimuthal angle and pseudorapidity are equal between the Ξ^- and both kaons. This result can be explained by uncorrelated remnants from two-particle correlations that have not been sufficiently corrected through mixed events. A biased simulation also provides us with an expected production mechanism favouring the production of the particles in the triplets close to each other in angular coordinates, raising the need for further analysis to improve event mixing corrections.

Popular Science Summary

Our world is made of matter composed of different layers, similarly to Matryoshka dolls. A material is made of atoms, which are made of smaller particles, such as electrons with negative charge or nucleons. Nucleons are either protons with positive charge or neutrons without charge. They are themselves made of smaller particles called quarks, which exist in different types in nature. Quarks cannot however exist freely, they are bound mainly in pairs or triplets called hadrons. The set of all the elementary particles (hence what we know are the smallest particles possible) is called the Standard Model.

Particles in the Standard Model are subject to different forces: the electromagnetic force, the weak force and the strong force. In the case of proton-proton collisions at high energies, such as the collisions happening at the LHC (Large Hadron Collider), the strong force dominates the other ones. In the strong interaction sector, the very high temperature reached during collisions allows the formation of the Quark Gluon Plasma (QGP), a state of matter similar to the early Universe medium. One key property of the QGP is strangeness enhancement, the production of a large number of strange quarks, which will then form hadrons.

When a quark is created, it has a twin sibling, an anti-quark, which shares the same mass but has an opposite charge. It is possible for bound particles to split following the Lund String Model: quarks combinations are assumed to behave like strings with particles at each end. Quarks' energies will transfer to string which will elongate further and further, until reaching a breaking point. Similarly to an elastic breaking, the quarks will be projected with high momenta. When encountering a quark that has been subject to the same phenomenon, a fleeing quark will once again bind with this new partner, creating a new hadron.

This thesis focuses on the study of strange flavoured hadrons. When a quark and anti-quark pair is separated through string breaking, the quarks remain correlated. The objective of our work is then to find which particle is correlated with which, hence finding which particles are created from the initial strange quark and anti-quark pair. This is achieved by studying angular correlations, namely how the angular coordinates of each particle behave with respect to each other.

In order to study particle correlations, we firstly in the thesis use simulated data. This

data set is obtained using the PYTHIA program, an event generator for high-energy collision events, based on the Lund String Model. Running simulations allows us to know precisely what particle is created during the proton-proton collision for a similar experimental process, hence providing us with what could be expected with real data. The real data analysis is performed with data provided by A Large Ion Collider Experiment (ALICE) from the LHC, located at CERN in Geneva, allowing us to study three-particle correlations with respect to strangeness.

Acknowledgements

First and foremost, I would like to thank my supervisor, Alice Ohlson, for giving me such an appealing subject and giving me the opportunity to work with you. Thank you for always taking the time to answer my questions and help me get on the right track. You have made working on this thesis a real pleasure, and I can't thank you enough for that. I would also like to thank Peter Christiansen for helping me understand the analysis codes better and how to face the real data sets.

I also want to thank my parents and my sister, who have unrelentingly supported me through not only this thesis but my studies in general. Thank you for always believing in me.

Contents

List of Acronyms

ALICE : **A** **L**arge **I**on **C**ollider **E**xperiment

BF : **B**alance **F**unction

CERN : **C**onseil **E**uropéen pour la **R**echerche **N**ucléaire (European Council for Nuclear Research)

COSPA : **COS**ine of the **P**ointing **A**ngle

DAQ : **D**ata **A**c**Q**uisition

DCA : **D**istance of **C**losest **A**pproach

EMCal : **E**lectro**M**agnetic **Cal**orimeter

HMPID : **H**igh **M**omentum **P**article **I**dentification **D**etector

LHC : **L**arge **H**adron **C**ollider

MC : **M**onte-**C**arlo

PDG : **P**article **D**ata **G**roup

PHOS : **PHO**ton **S**pectrometer

QCD : **Q**uantum **C**hromo**d**ynamics

QED : **Q**uantum **E**lectro**d**ynamics

QGP : **Q**uark **G**luon **P**lasma

TPC : **T**ime **P**rojection **C**hamber

TOF : **T**ime **O**f **F**light

TRD : **T**ransition **R**adiation **D**etector

OSOS : **O**pposite **S**ign **O**pposite **S**ign

OSSS : **O**pposite **S**ign **S**ame **S**ign

SSOS : **S**ame **S**ign **O**pposite **S**ign

SSSS : **S**ame **S**ign **S**ame **S**ign

1 Introduction

Proton-proton or nucleus-nucleus collisions at high energies such as the ones happening at the LHC (Large Hadron Collider) result in the production of partons and hadrons. Although the valence quarks of the protons are only up and down quarks, the production of strange-flavoured hadrons has been observed [1]. Strangeness production can be explained with string breaking theories based on the Lund string model [2] or through strangeness enhancement in the Quark Gluon Plasma, a state of matter similar to the early Universe medium [3]. The microscopic mechanisms underlying the production of strange-antistrange $s\bar{s}$ pairs, and their subsequent hadronisation, is still an active area of research in both small and large collision systems. The requirement for strangeness to be conserved in the strong force induces correlations between strangeness-balancing hadrons produced in the same process.

The motivation for this thesis is to deepen our knowledge on the production of strange quarks by studying the angular correlations between a Ξ^- baryon (dss) and two K^+ mesons ($u\bar{s}$), by focusing on the azimuthal angle and the pseudorapidity parameters. Since three-particle correlations are affected by the two-particle correlations residuals, our study requires the use of balance functions. This analytic tool will allow us to remove charge-independent effects as well as uncorrelated triggers through event mixing, in order to observe how the strangeness is balanced in the ($\Xi^- K^+ K^+$) triplet. Such an analysis could tell what is the most probable way of balancing strangeness, which can then motivates the analysis of other strange triplets or pairs.

First, simulations using the PYTHIA program to generate high-energy collision events will be run in section 4.1, before using data from ALICE (A Large Ion Collider Experiment) in section 4.2 to try to corroborate our Monte-Carlo simulated results and describe the strangeness behaviour due to its conservation.

2 Theory

2.1 The Standard Model

The Standard Model describes the set of all elementary particles. It is composed of two categories. The first one contains particles called fermions, which is itself divided into three generations or families. Each generation includes a positively charged quark, a negatively charged quark, a lepton and a neutrino. Every fermion has its corresponding anti-particle, with the same mass or spin, but opposing charge. The stable matter in the Universe is only composed of fermions from the first generation : up quarks, down quarks and electrons. Particles composed of quarks from the second and third generations still exist, but they are unstable and may have a very short lifetime, hence they decay extremely quickly [4]. The other category of particles in the Standard Model are bosons, the interaction/force carriers. The photon γ is the mediator of the electromagnetic (EM) force, whose interactions are described in the Quantum Electrodynamics (QED) theory. The $W^{\pm}$ and the Z^0 bosons are the mediators of the weak force. Those two forces have been unified in the electroweak gauge group theory of the Standard Model [4].

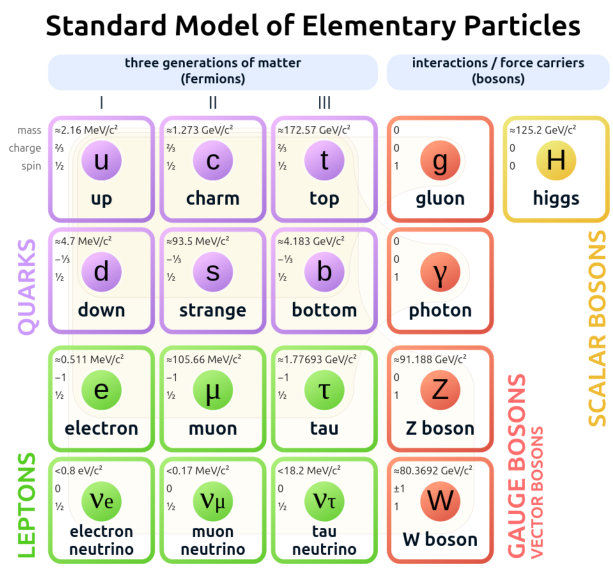

Figure 2.1: Standard Model of Elementary Particles (from [5])

The gluon g is the mediator of the strong force, hence being applied in the strong sector or Quantum Chromodynamics (QCD). The gluon interacts with coloured particles such as quarks, which have a quantum number corresponding to either blue, red or green (anti-blue, anti-red or anti-green for anti-particles). Because of this specific quantum number, quarks are confined in hadrons, a set of quarks, as a particle has to be colourless to exist. Therefore no quarks can exist freely, and they are bound mainly in baryons (qqq or $\bar{q}\bar{q}\bar{q}$) or mesons ($q\bar{q}$).

The three particles of interest in this study are a Ξ^- baryon and two K^+ mesons, respectively a dss baryon and two $u\bar{s}$ mesons (see table 2.I). To study the production mechanisms of the ($\Xi^- K^+ K^+$) triplet, we have to ensure quantum numbers balancing.

Particle	Antiparticle	Quarks	S	B	Q	Mass [MeV/c^2]	Mean Life[s]	Decays	PDG
Ξ^-	Ξ^+	dss	-2	+1	-1	1321.71 ± 0.07	1.639 ± 0.015 10^{-10}	$[\Lambda, \pi^-]$	3312
								$[\Sigma^-, \gamma]$	
								$[\Lambda, e^-, \bar{\nu}_e]$	
K^+	K^-	$u\bar{s}$	+1	0	+1	493.677 ± 0.015	1.2380 ± 0.0020 10^{-8}	$[\pi^+, e^-, \bar{\nu}_e]$	321
								$[\pi^+, \mu^-, \bar{\nu}_\mu]$	

Table 2.I: Properties of the Ξ^- baryon and K$^+$ meson (from [6])

Particles in the Standard Model have corresponding quantum numbers. For instance, both the baryon and the mesons of interest have a number corresponding to strangeness, S, that has to be conserved in the strong and EM interaction.

$$S = n_{\bar{s}} - n_s \tag{2.1}$$

Another quantum number that is not discussed here is the baryon number B, that must also be balanced. It is defined as

$$B = \frac{1}{3}(n_q - n_{\bar{q}}) \tag{2.2}$$

The Ξ^- is a baryon, and therefore has a B number equal to 1 (see tale 2.I). Therefore, for the baryon number to be balanced, there should be a particle with B = -1, an anti-baryon. The minimally balancing combination would involve an anti-proton $\bar{p} = \bar{u}\bar{u}\bar{d}$, that would at the same time balance the d-quark from the Ξ^- and the two u-quarks from the K^+. The Ξ^- baryon could also be correlated to other hyperons (baryons that contain at least one strange quark but no charm quark or any quark from the third generation) such as a $\bar{\Lambda}$ ($\bar{u}\bar{d}\bar{s}$ with a K^+, or its own anti-particle Ξ^+. These two combinations would ensure the baryon balancing inside the triplet and the doublet.

2.1.1 Strangeness Production and The Quark-Gluon Plasma

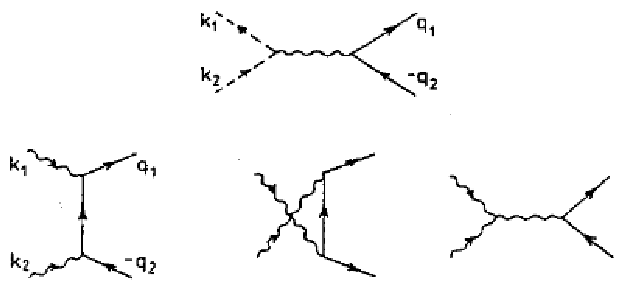

Figure 2.2: Strangeness production mechanisms from [7]. The top Feynman diagram represents $q\bar{q} \to s\bar{s}$ production mechanism. Bottom diagrams represent $gg \to s\bar{s}$ mechanisms

In QCD, gluons can undergo partonic processes resulting in the formation of strange quarks. The $s\bar{s}$ pair can be produced by annihilation of quark-antiquark pairs and in two-gluons collision in lowest order perturbative QCD (see figure 2.2). The respective cross-sections for these processes are :

$$\bar{\sigma}_{q\bar{q}\to s\bar{s}} = \frac{8\pi\alpha_s^2}{27s}\left(1+\frac{2M^2}{s}\right)w(s) \tag{2.3}$$

$$\bar{\sigma}_{gg\to s\bar{s}} = \frac{2\pi\alpha_s^2}{3s}\left[\left(1+\frac{4M^2}{s}+\frac{M^4}{s^2}\right)\tanh^{-1}w(s)-\left(\frac{7}{8}+\frac{31}{8}\cdot\frac{M^2}{s}\right)w(s)\right] \tag{2.4}$$

where ($s\bar{s}$) represents the formed strange-antistrange pair, s is the invariant mass squared such that $s=(k_1+k_2)^2$ with k_i the four momenta of the incoming particle. α_s is the effective QCD coupling constant $\alpha_s = \frac{g^2}{4\pi} \approx 0.6$ and $w(s)$ is such that $w(s) = (1-\frac{4M^2}{s})^{\frac{1}{2}}$ [7].

Analyses of heavier ions than proton have allowed the discovery of a phase of QCD called the QGP(Quark-Gluon Plasma), similar to the early Universe medium [3], for high temperature collisions, with resulting temperatures above 150 to 160 MeV (equivalent to $10^{12}K$ [8]). At this temperature, quarks and gluons are no longer confined in hadrons, facilitating the partonic processes presented above. Because of the Pauli exclusion principle that states that two particles with same quantum numbers cannot exist simultaneously in a same quantum state, the creation of $s\bar{s}$ pairs is favoured: as the proton has u and d valence quarks, their initial abundance suppresses the production of $u\bar{u}$ and $d\bar{d}$ pairs, unlike the production of $s\bar{s}$ pairs. This large-scale production of strange flavoured quarks is known as strangeness enhancement, which is a feature of the QGP [4, 9], but has also been observed in pp collisions [1].

2.2 Particle detection at the ALICE detector

The ALICE detector is located at the Large Hadron Collider (LHC) at CERN, in Geneva (figure 2.3). It is optimised for identification and precise tracking of particles, especially in the high-multiplicity environment of heavy-ion collisions [10]. The LHC focuses on proton-proton collisions measured at $\sqrt{s} = 13$ TeV, lead-lead (Pb-Pb) collisions at $\sqrt{s_{Pb-Pb}} = 5.02$ TeV or proton-lead (p-Pb) collisions at $\sqrt{s_{p-Pb}} = 8.16$ TeV [11].

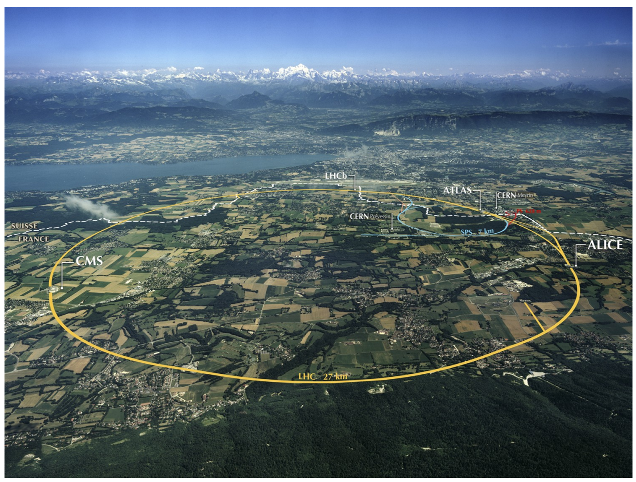

Figure 2.3: Aerial view of the LHC area (from [12])

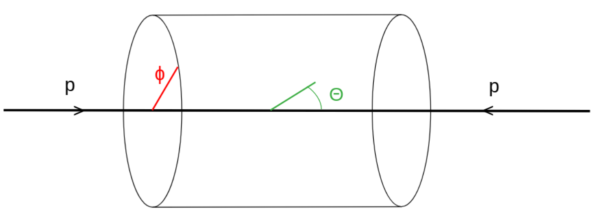

Figure 2.4: Scheme of the detector with angles of interest

In particle collisions, polar coordinates are used to measure the direction of a track. The azimuthal angle ϕ is the angle in the plane perpendicular to the beam axis, while θ is the longitudinal angle, relative to the beam , as shown in figure 2.4. Each particle produced in a high-energy hadron-hadron interaction has a transverse momentum p_T in the plane transverse (perpendicular) to the beam. The 4-momentum of such a product can be expressed as (from [4]):

$$p = (E, p_T \cos\phi, p_T \sin\phi, p_z) \tag{2.5}$$

A useful parameter in the study of formed particles is the rapidity y, defined as :

$$y = \frac{1}{2} \ln\left(\frac{E + p_z}{E - p_z}\right) \tag{2.6}$$

In the high-energy or relativistic limit, the rapidity can be approximated by the pseudorapidity η:

$$\eta = \frac{1}{2} \ln\left(\frac{1 + \cos\theta}{1 - \sin\theta}\right) = -\ln\tan\left(\frac{\theta}{2}\right) \tag{2.7}$$

We therefore have for our analysis frame $\Delta y \equiv \Delta\eta$. The use of the difference is pseudorapidity $\Delta\eta$ instead of the pseudorapidity itself as one of our study parameter is motivated by the invariance property under a Lorentz transformation of Δy, with the same property hence applying to $\Delta\eta$.

2.2.1 Detector layout

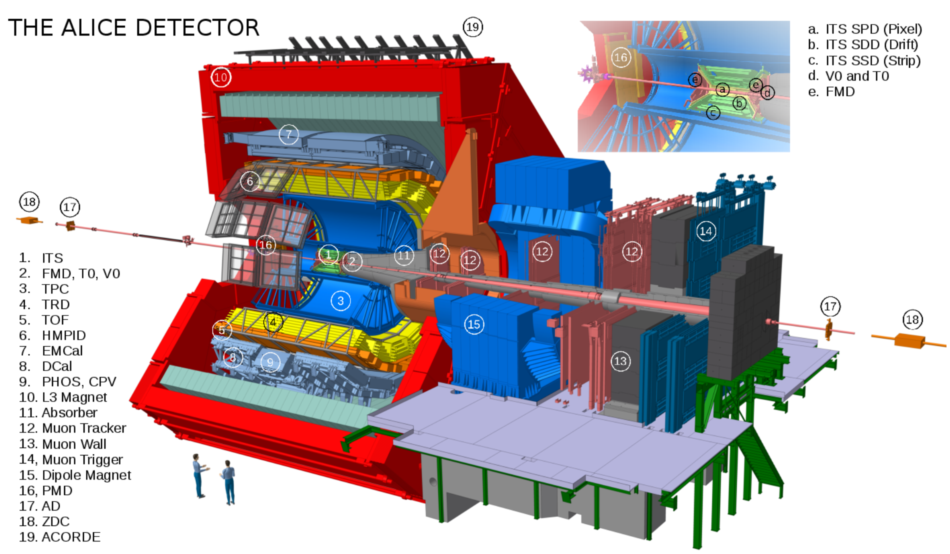

Figure 2.5: Representation of the ALICE detector during Run2 (from [13])

The ALICE experiment is a set of numerous sub-detectors with a total size of $16\times16\times26$ m^3 [10]. The central-barrel detectors are surrounded by the L3 solenoid magnet, inherited from the same name experiment which was part of the Large Electron-Positron (LEP) collider [14]. The ALICE detector sits in the cavern where the L3 used to be at Point 2 (see figure 2.3), reusing the previous experiment's red octagonal magnet, visible in figure 2.5. It provides a magnetic field of B = 0.5 T to the central-barrel detectors. The pseudorapidity acceptance is such that $|\eta| < 0.9$, which corresponds to a longitudinal angle of 45°. Precise momentum determination and tracking is possible down to $p_T > 0.15$ GeV/c. It is composed of the Inner Tracking System (ITS), the Time Projection Chamber (TPC), the Transition Radiation Detector (TRD), the Time-Of-Flight (TOF) detector, the Photon Spectrometer (PHOS), the Electromagnetic Calorimeter (EMCal) and the High Momentum Particle Identification Detector (HMPID) [15]. The detector layout discussed below corresponds to ALICE's configuration during Run 2, since the results presented in section 4.2 originate from data collected in 2017 and 2018. Since we focus primarily on data from the ITS, the TPC, the TOF and the V0 detector in our analysis, we will first present these sub-detectors, before taking a glance at the remaining central-barrel detectors, the triggering system and the data acquisition system.

The **ITS**, along with the TPC, is one of the main charged-particle tracking detectors. It is composed of two Silicon Pixel Detectors (SPD), two Silicon Drift Detectors (SDD) and two Silicon Strip Detectors (SSD), making up six tracking layers. The set of silicon detectors is able to cover the full azimuthal range and the pseudorapidity range of $|\eta| < 0.9$ for all tracks that stray away from the beam direction by one absolute standard deviation $\pm\ 1\sigma$ (or $\pm$ 5.3 cm). The first SPD layer covers the pseudorapidity range $|\eta| < 1.98$, which allows to measure the multiplicity of charged-particles over a continuous range. Its main task is to localise with precision the primary vertex, then reconstruct the secondary vertices from hyperons and D and B mesons, as well as identifying and tracking particles with momentum below 200 MeV/c. The four outer layers of the ITS, the two SDD and SSD, provide the experiment with charged particle identification in the non-relativistic region by measuring the specific ionisation energy loss dE/dx [15, 10]. The ITS was upgraded to its second version, the ITS2, for Run3, which started in 2021 and is still the current run, until the third LHC long shutdown scheduled at the end of July of this year. A new upgrade, ITS3, is currently in the works to be installed at the beginning of Run4, scheduled in 2029 [16].

The **TPC** is designed to provide good two-track separation, charged particle momentum measurement, particle identification and vertex determination in the region $p_T < 10$ GeV/c for hadronic and leptonic signals [17]. It consists of a field cage equipped with a drift gas system and two end readout chambers, closed by a gating grid and calibrated by a laser system [10]. It covers the full azimuthal range, and the pseudorapidity range $|\eta| < 0.9$ for full radial track length. A larger pseudorapidity range is covered ($|\eta| < 1.5$) for reduced track length of approximately 1/3 of the full track length. Similarly to the ITS, particle identification is performed via specific ionisation energy loss $\mathrm{d}E/\mathrm{d}x$ measurements. A $\mathrm{d}E/\mathrm{d}x$ resolution of 8% is necessary for good hadron identification. The detector is designed to have a great track matching capability with the ITS, the other main charged particle tracking detector. A matching efficiency between 85 and 95 % is necessary for multi-strange baryons measurements [17]. The TPC will be useful for our kaon identification, along with the TOF.

The **TOF** is designed for Particle IDentification (PID), and specialised in the identification of long-lived hadrons, mainly pions, kaons and protons [18]. The detector is composed of multiple Multi-gap Resistive-Plate Chamber (MRPC), placed inside a cylindrical shell filled with gas. It covers the same pseudorapidity range as the ITS and the TPC, $|\eta| < 0.9$,as well as covering the full azimuthal range. The detector is designed to avoid any loss in the sensitive area, but one dead area along the z-axis is caused by the presence of a supporting space frame structure that cannot be removed. The momentum range covered by the TOF varies for the type of particle: between 0.3 and 3.0 GeV/c for kaon and pion identification, and between 0.5 and 6.0 GeV/c for proton identification. Positive and negative particles can be distinguished from their curvature in the detector. Because of its importance for kaon identification, the TOF will be useful in the rest of this thesis, as discussed later in section 3.2.2.

The multiplicity is measured thanks to the **V0** detector, composed of two arrays of scintillators, V0A and V0C, respectively located at the front, 340 cm from the interaction point, and at the back, 90 cm from the interaction point. They have different inner and outer radii, respectively 2.3 and 42.2 cm for the V0a scintillator, and 4.5 and 32 cm for the V0C scintillator [11]. Each scintillator is divided into 8 azimuthal sector and 4 radial sectors, covering a different pseudorapidity range: V0A covers the range $2.8 < \eta < 5.1$ and V0C covers the range $-3.7 < \eta < -1.7$. This layout allows the V0 to provide information on the centrality or multiplicity of the collision. The detector also stands as a minimum-bias trigger for the central barrel detectors or measuring the luminosity in pp collisions [10, 11]. As the multiplicity is related to the centrality of an event, it is determined using the V0A and the V0C scintillators arrays. The multiplicity is extracted from the V0M, which corresponds to the summed amplitude in the V0A and V0C forward-rapidity scintillators [11].

The **TRD**'s purpose is to provide electron identification for momenta above 1 GeV/c. Electrons with lower momentum are identified in the TPC by energy loss measurement. The TRD, with data from the ITS and the TPC, has made it possible to reconstruct open charm and open beauty in semi-leptonic decays, such as Υ or J/Ψ [19].

The **HMPID**, as its name indicates, allows the identification of particles with higher momenta than the range of the ITS, TPC and TOF. It increases the identification range of the π/K and K/p discrimination to respectively 3 GeV/c and 5 GeV/c, while also allowing the identification of light nuclei and anti-nuclei at high p_T, such as deuterons, tritons, helium-3 nuclei and alpha particles. The HMPID is however not the main detector used for PID, as it covers only 5% of the angular coverage of the central barrel detectors [10].

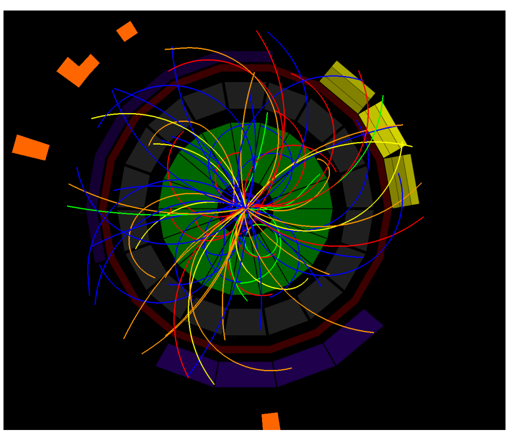

Figure 2.6: From [20], a pp collision at 13 TeV seen by ALICE during Run 2 in 2016. Blue tracks are electrons, green tracks are muons, red tracks are pions, orange tracks are protons and yellow tracks are kaons.

The **PHOS** is a high-resolution electromagnetic spectrometer. It allows, thanks to measurement of high-p_T π^0 and photons, the study of jet quenching, as well as the study of the initial phase of the collisions [10].

The **EMCal** is a Pb-scintillator calorimeter in the central barrel. The role of a calorimeter is to measure the energy of a jet by observing energy showers. The detector provides an electronic signal proportional to the energy deposited in the calorimeter, allowing us to identify and reconstruct particles [4, 10]. In order to extend the acceptance range of the EMCal, a Di-Jet Calorimeter (DCal) upgrade has been added to the calorimeter system. It enabled back-to-back correlation measurements, allowing a full understanding of the events in the EMcal [21].

2.2.2 Triggering system and data acquisition

As some particles are very short lived, their identification is done through the reconstruction of their decay products, a method referred to as V^0 decay reconstruction. It is the case for the Ξ^- baryon, for which we reconstruct a π^- and a Λ^0 (see 2.I). The latter will then decay further to a proton and a π^-, as shown in figure 2.7. Three parameters need to be introduced for the reconstruction analysis. The first one is the Distance of Closest Approach (DCA), which corresponds to the distance between the primary vertex (found with the ITS and the TPC) and the reconstructed particle paths. Tracks with unlike-sign pairs are chosen as V^0 candidates, and the point of closest approach between the two tracks is then calculated [15]. Tracks that have a DCA to the primary vertex greater than a certain value are selected. The second is the cosine of the pointing angle (COSPA), which corresponds to the angle between the line connecting the V^0 vertex and the primary vertex, and the V^0 momentum. The pointing angle corresponds to θ in figure 2.7. Cuts on the COSPA value ensure that only candidates with momentum pointing from the primary vertex are selected [22]. The third parameter is the radius, which corresponds to the distance between the primary vertex and secondary (or primary and tertiary) vertices in the transverse plane [15]. Figure 2.8 shows the treatment of an event in the ALICE detector (from [11, 23]).

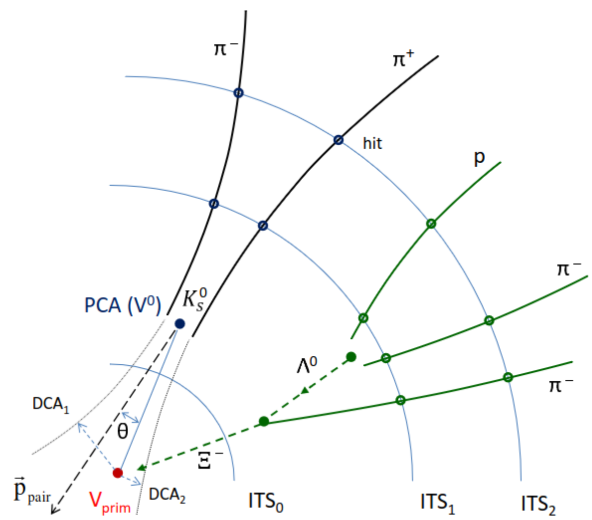

Figure 2.7: Secondary vertex reconstruction principle from [15]

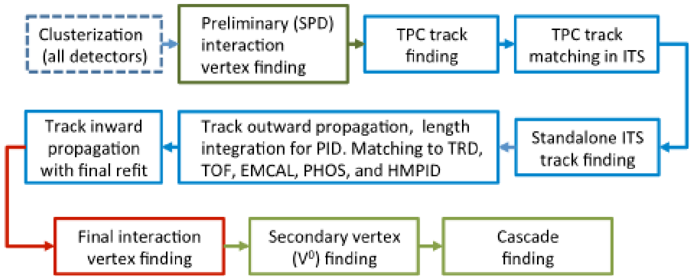

Figure 2.8: Diagram of an event treatment in the ALICE detector (from [11, 23])

The ALICE experiment is also equipped with a Central Trigger Processor (CTP) to select events meeting the requirements of the detectors in the central barrel, the muon spectrometer and the forward detectors. It is designed to account for the different multiplicity of Pb-Pb, p-A and p-p collisions [10].

If an event passes through the V0 and the CTP triggers, it is sent to the Data AcQuisition (DAQ) system, which will perform a last cut to select if the event is recorded or not. It must be able to acquire a large fraction of rare events while balancing the capacity of the experiment to record central collisions that generates large events.

2.3 PYTHIA

PYTHIA is a Monte-Carlo (MC) event generator [2]. It simulates proton-proton collisions at a certain center of mass energy, specified while launching the code. It allows the reproduction of collisions similar to the ones taking places at the LHC, based on the Lund String Model theory.

2.3.1 Lund String Model

The Lund String Model relies on representing a quark-antiquark pair as a string, with the two particles at each end. The potential energy of the quarks will be transmitted to the string, until it reaches a limit point. The string will then break, creating new quark-antiquark (or diquark-antidiquark) pairs, and both particles will be ejected with a certain momentum. As stated above, a quark cannot exist freely and has to be confined in a hadron, and will therefore be bound with another quark originating from another string breaking phenomenon

[2]. This process allows the creation of new particles, such as in the example in figure 2.9.

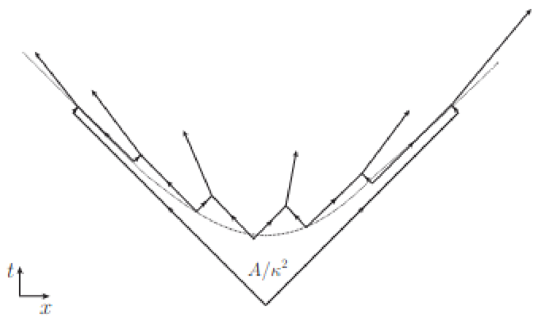

Figure 2.9: String breaking mechanism (figure 14.b from [2])

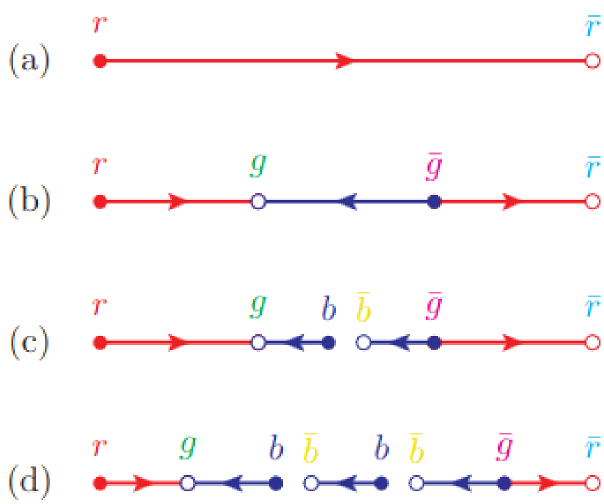

Figure 2.10: Example of the popcorn mechanism (from [24])

There is however a subtlety in how PYTHIA works that allows us to obtain a better understanding of the three particle correlations we are working with, called the popcorn mechanism. The creation of a string in PYTHIA does not necessarily imply the breaking of that same string. If a string contains two different colour singlets, the virtual fluctuation can be formed before being annihilated [24]. Figure 2.10 shows that a virtual green-antigreen $q\bar{q}$ pair can be formed on the string spanned by a red-antired $q\bar{q}$ pair. The field between the virtual particles will become antiblue-blue. As shown in (b), the colour flow in that part of the string is reversed, and the force acting on the green quark is zero, preventing string breaking. The string breaks in (c) with the formation of a blue-antiblue pair. The original string is now divided into two parts, with diquarks at the end (baryons are formed). If the string breaks again in the blue field, the creation of a meson is possible, as shown in (d). This explains how a $(\Xi^- K^+ K^+)$ triplet can be formed in PYTHIA, with the baryon number balanced by a non-strange anti-baryon (for instance an anti-proton).

3 Method

3.1 MC generation

Using PYTHIA 8.315 [2], we generate collision events that we store in several ROOT [25] trees, that will then be combined into a chain in order to obtain a large number of samples. The elastic and inelastic processes, single double and central diffractive and non diffractive processes are included, and particles are stopped from decaying weakly, since they can be reconstructed via their secondary vertex (only particles with proper lifetime $\tau <$ mm$/c$ are allowed to decay). In order to so, the following flags are used [2]:

```
pythia.readString("ParticleDecays:limitTau0=on");
pythia.readString("ParticleDecays:tau0Max=10");
```

All trees are generated with a center-of-mass energy of 13 TeV. They contain information such as the pseudorapity η and the azimuthal angle ϕ, but also the multiplicity of each event and the PDG code of each produced particle. The later will allow us to identify the particles, with PDG(Ξ^-) = 3312 and PDG($K^\pm$) = $\pm$ 321 [6]. Using the ROOT framework will then allow us to plot the ($\Xi^- KK$) three-particle correlation functions.

3.1.1 Biased verification

As explained above, the particles of interest are selected thanks to their PDG code. We can extend this method by applying some conditions on the event generation. Another simulation is run with a strong bias where we select an event for analysis only if the strangeness on the string is balanced through the Ξ^- and two positive kaons. The strangeness can not be located at the ends of the strings, and no other strange-flavoured particle is allowed. The number of non-strange particles is however not restricted. One example of such a string is presented below :

$$\pi^- — \pi^0 — \rho^+ — \eta — \pi^- — \pi^+ — \pi^0 — K^+ — \Xi^- — K^+ — \bar{\Delta}^- — \pi^+$$

In this example, the strangeness of the Ξ^- is balanced by the two K^+ mesons, and the baryon number is balanced by the $\bar{\Delta}^-$. Creating such events and plotting the correlation for both the difference in azimuthal angle and pseudorapidity allows us to understand better the previously obtained simulated results, as we can ensure how the strangeness is balanced. Moreover, the bias certifies that the three particles are produced in the same process, so no correction is needed for the results.

It is still necessary to rely on the generated events from section 3.1, as they are expected to be more representative to the real data results, where no such strong bias can be applied.

3.2 Real Data selection

Unlike in the simulated data, we are not able to select particles using their PDG code in real data. We then have to select the particles of interest by performing cuts on measured particle properties. The performed cuts are presented in table 3.I. ΔM_Λ and ΔM_{Ξ^-} correspond to the difference between the invariant mass and the known mass of the particle, here the mass of the Λ and the mass of the Ξ^- respectively (see table 2.I). The invariant mass value is explained in section 3.2.1. Only the standard cut variation presented in table 3.2.1 was used to obtain to produce our ROOT trees, but the very loose and tight variation can be used in a future systematic uncertainty estimation.

3.2.1 Ξ^- selection

To obtain an estimate of which particles in our data set is a Ξ^-, we will plot the distribution of $\Delta M = M_{Inv} - M_{\Xi^-}$ as a function of the transverse momentum p_T. For a particle with two daughter particles 1 and 2, the invariant mass M_{Inv} is defined in equation 3.1, where $m_{1,2}$ $\vec{p_{1,2}}$ and $E_{1,2}$ are the masses, the momentum vectors and the energies of the daughter particles [26].

$$\begin{aligned} M_{Inv} &= m_1^2 + m_2^2 + 2(E_1 E_2 - \vec{p_1} \cdot \vec{p_2}) \\ M_{Inv} &= m_1^2 \left(\frac{1+p_2}{p_1}\right) + m_2^2 \left(\frac{1+p_1}{p_2}\right) + 2p_1 p_2 (1 - \cos\theta) \end{aligned} \tag{3.1}$$

Cuts that are not varied			
$\lvert\Delta M_{\Xi^-}\rvert$ (GeV/c^2)	< 0.1		
Pseudorapidity	$\lvert\eta\rvert < 0.8$		
Transverse momentum (GeV/c)	$0.15 < p_T < 7.0$		
Cascade radius (cm)	> 0.8		
DCA V0 daughters (cm)	< 1.6		
V0 radius (cm)	> 1.4		
Cut variation	**Very Loose**	**Standard**	**Tight**
cascDCA (cm)	> 1.9	> 1.6	< 1.5
cascCOSPA	< 0.95	< 0.97	> 0.98
$\lvert\Delta M_\Lambda\rvert$ (GeV/c^2)	> 0.006	> 0.006	< 0.005
V0DCA (cm)	< 0.07	< 0.07	> 0.08
V0COSPA	< 0.92	< 0.97	> 0.97
bachDCA (cm)	< 0.03	< 0.05	> 0.05
posDCA (cm)	< 0.02	< 0.05	> 0.05
negDCA (cm)	< 0.02	< 0.05	> 0.05

Table 3.I: Values used for generation of root trees for three different cut variations

A peak is centred at 0 as shown in figure 3.1, as the value of ΔM should be 0 when the mass of the Ξ^- candidate matches the know mass of the Ξ^- from [6]. We can then select limits in the difference in mass for which we consider the particle to be a Ξ. However, we still need to get rid of some combinatorial background, which are random proton-pions ($p\pi\pi$) triplets that have a similar mass. Those "fake Ξs" are part of the peak region, so in order to remove their contributions, we will perform a polynomial fit on both sides of the determined Ξ area, giving us an estimated percentage of background triplets in our peak region. We compute the correlation function for the fake Ξ candidates on the left and on the right-hand side, which are then normalised by the ratio of signal and background. The fit is performed separately for the left and right-hand sides of the Ξ^- peak as the number of fake Ξ candidates varies between the two regions. The background is subtracted from the determined Ξ signal region to obtain an estimate of the number of Ξ baryons in the sample.

p_T range (GeV/c)	0.60 - 1.20	1.20 - 1.60	1.60 - 2.20	2.20 - 2.80	2.80 - 3.60	3.60 - 5.00	5.00 - 6.50
Fake percentage from Left side	15.3 %	11.4 %	10.5 %	8.3 %	6.9 %	5.8 %	4.8 %
Fake percentage from Right side	13.7 %	10.2 %	9.4 %	7.5 %	6.2 %	5.5 %	4.7 %

Table 3.II: Percentage of fake Ξ^- in the peak according to different p_T bins

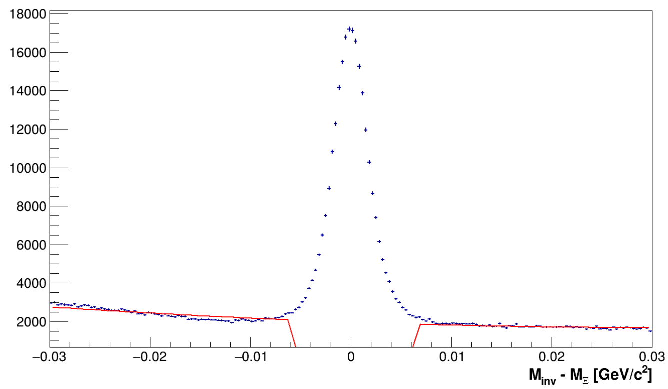

Figure 3.1: Fit on the Invariant mass plot for p_T = 0.6 - 1.2 GeV/c

The left side corresponds to the range in the peak region -0.006 to 0 in the x-axis and the right side corresponds to the range in the peak region from 0 to 0.006. The fit has been calculated taking into account values from -0.02 to 0.02.

We observe from table 3.I that for higher transverse momentum, fewer random $p\pi\pi$ triplets are present in the peak region, and therefore the percentage of real Ξ^- is higher.

The performed fit also allowed us to check the necessity for such a method. From the same table 3.I, we observe that for lower p_T, we observe that the percentage of "fake" Ξ^- is significant and that a subtraction is needed to obtain valid results in the correlations and balance functions.

3.2.2 Kaon selection

To select which particles are kaons, we need to analyse the results from the Time Projection Chamber (TPC) and the Time Of Flight (TOF) detectors (see section 2.2.1). We plot for both detectors the distribution of respective $n\sigma$ as a function of the transverse momentum, where $n\sigma$ is the number of standard deviations from the Bethe-Bloch parametrisation of the TPC and the TOF [27]. We make projections for each momentum bin, which provide us with 1-dimensional graphs (see figure 3.3). Three peaks are seen, one corresponding to pions, one to kaons and one to protons. We then make cuts around the kaon peak to select the particles of interest. For the lower momentum bins, we use the TPC data. As the momentum increases, the pion band and the kaon band will merge, preventing us from determining a kaon region. This forces us to switch to the TOF data, until once again the two peaks merge.

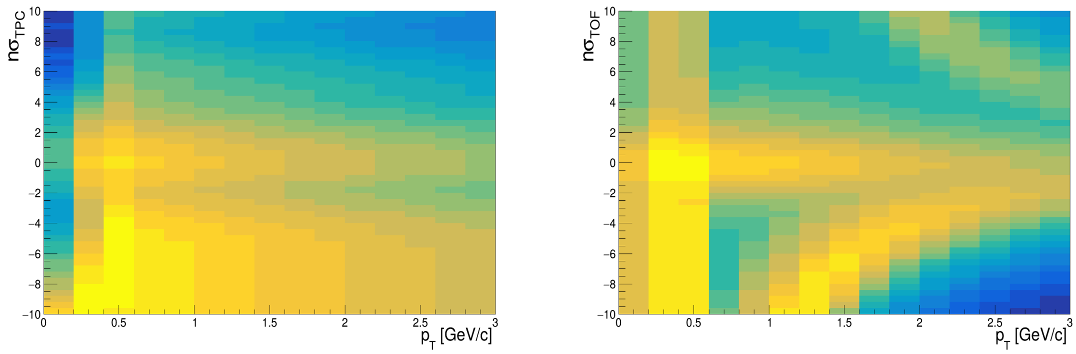

(a) TPC results (b) TOF results

Figure 3.2: TPC and TOF results as a function of p_T between -10 and 10 σ

By performing the projections on the y axis such as presented in figure 3.3, we are able to set a $n\sigma$ range to determine kaons from pions and protons. We are able to tell particles apart using the TPC up to a momentum of 0.6 GeV/c^2, and for the TOF up to 2.4 GeV/c^2. We can note that the higher the transverse momentum, the closer the pion peak and the kaon peak are, and therefore the smaller the $n\sigma$ range is. The transverse momentum range matches the expected limit for the TPC and the TOF particle identification presented in section 2.2.1.

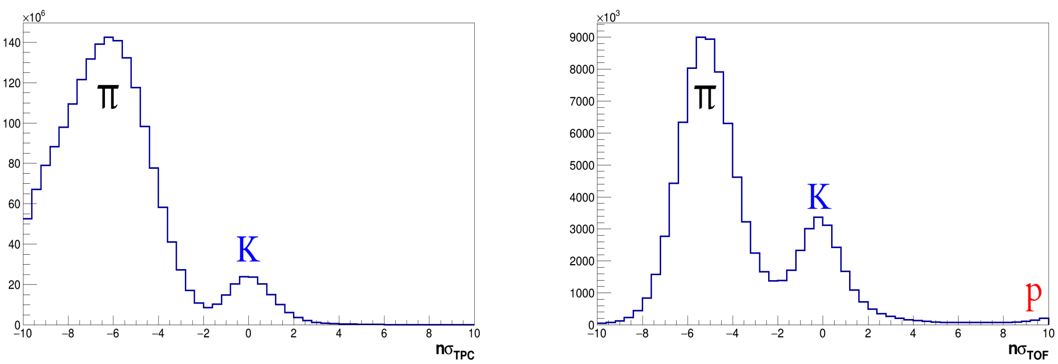

(a) TPC projection for p_T = 0.4 - 0.6 GeV/c (b) TOF projection for p_T = 1.6 - 1.8 GeV/c

Figure 3.3: Examples of TPC and TOF projections

	TPC		TOF							
p_T range (GeV/c)	0.15 - 0.4	0.4 - 0.6	0.6 - 0.8	0.8 - 1.0	1.0 - 1.2	1.2 - 1.4	1.4 - 1.8	1.8 - 2.0	2.0 - 2.2	2.2 - 2.4
$n\sigma$ range	[-3 ; 4]	[-2 ; 4]	[-5 ; 6]	[-4 ; 6]	[-3 ; 6]	[-2.5 ; 6]	[-2 ; 6]	[-1.5 ; 5]	[-1.5 ; 4]	[-1 ; 4]

Table 3.III: $n\sigma$ ranges according to different p_T bins

3.3 Particle Correlations

In order to understand particle production mechanisms, we study particle correlations, as they contain crucial information on collectivity [28], as well as information on the behaviour of particles relative to one another in angular or momentum space. Such an analysis consists in observing certain parameters behaviour with respect to each other, namely variables introduced in section 2.2.1, and plotting their distributions.

3.3.1 Two particle correlation functions

The correlation function for two particles is defined as

$$C^{(2)}(\Delta\phi, \Delta\eta) = \frac{1}{N_{pairs}} \cdot \frac{d^2 N_{pairs}}{d\Delta\phi d\Delta\eta} \tag{3.2}$$

where N_{pairs} corresponds to the number of trigger-associated particle pairs [29], Ξ^- being the trigger particle in our analysis, and $\Delta\eta$ and $\Delta\phi$ correspond to the difference in azimuthal angle and pseudorapidity between the trigger and the associated particle. We will in our analysis normalise to the number of triggers N_{trig}, as the per-trigger yield is the average number of associated particles at a given relative distance ($\Delta\phi$,$\Delta\eta$) to the determined trigger particle:

$$C^{(2)}(\Delta\phi, \Delta\eta) = \frac{1}{N_{trig}} \cdot \frac{d^2 N_{pairs}}{d\Delta\phi d\Delta\eta} \tag{3.3}$$

To obtain the two-particle correlation function, we compute the difference in azimuthal angle and in pseudorapidity for a Ξ^- and a kaon. The result can then be analysed in one dimension for the chosen parameter, or in two dimensions with $\Delta\phi$ on the x-axis and $\Delta\eta$ on the y-axis using the TH2 class from ROOT [30]. The result is normalised by the number of Ξ baryons, as in (3.3).

3.3.2 Three particle correlation functions

The expression in (3.3) can then be expanded to three particles A, B and C [31], where A is the trigger particle:

$$C^{(3)}(\Delta\phi_{A,B}, \Delta\phi_{A,C}, \Delta\eta_{A,B}, \Delta\eta_{A,C}) = \frac{1}{N_{trig}} \cdot \frac{d^4 N_{triplets}}{d\Delta\phi_{A,B} d\Delta\phi_{A,C} d\Delta\eta_{A,B} d\Delta\eta_{A,C}} \tag{3.4}$$

As the result of this correlation function is 4-dimensional, one would instead study the three particle correlations with respect to the difference in azimuthal angle and the pseudorapidity separately, providing us with:

$$\begin{aligned} C^{(3)}(\Delta\phi_{A,B}, \Delta\phi_{A,C}) &= \frac{1}{N_{trig}} \cdot \frac{d^2 N_{triplets}}{d\Delta\phi_{A,B} d\Delta\phi_{A,C}} \\ C^{(3)}(\Delta\eta_{A,B}, \Delta\eta_{A,C}) &= \frac{1}{N_{trig}} \cdot \frac{d^2 N_{triplets}}{d\Delta\eta_{A,B} d\Delta\eta_{A,C}} \end{aligned} \tag{3.5}$$

The result is a plot with the difference in the according parameter between the Ξ^- and the first kaon on the x-axis, and the difference between the Ξ^- and the second kaon on the y-axis. The distribution is then normalised by the number of triggers, as in (3.5).

3.3.3 Balance functions

In order to study the correlations between the Ξ^- baryon and the two K^+ kaons, we have to investigate other particle combinations that are produced in the same process. Indeed, some residuals are present in the correlation function for the triplet $(\Xi^- K^+ K^+)$, such as two-particles correlations, with the third particle being uncorrelated. Correlation functions contain charge-independent as well as charge-dependent effects, and the role of the Balance Function (BF) is to isolate the charge-dependent ones by subtracting the charge-independent effects.

To obtain the balance function for $(\Xi^- K^+ K^+)$, we have to compute the correlation functions for different combinations of the kaon charge. Hence we will compute the correlation function for $(\Xi^- K_1^+ K_2^+)$, $(\Xi^- K_1^+ K_2^-)$, $(\Xi^- K_1^- K_2^+)$ and $(\Xi^- K_1^- K_2^-)$, where K_1 and K_2 are numbered to differentiate the two kaons, but the indices do not carry any physical meaning. Each combination is composed of the following correlations, where parenthesis represent particles produced in the same process:

$$\begin{aligned}
C_1^{(3)}\,(\Xi^- K_1^+ K_2^+) &= (\Xi^- K_1^+ K_2^+) + (\Xi^- K_1^+) K_2^+ + (\Xi^- K_2^+) K_1^+ + \Xi^- (K_1^+ K_2^+) + \Xi^- K_1^+ K_2^+ \\
C_2^{(3)}\,(\Xi^- K_1^+ K_2^-) &= (\Xi^- K_1^+) K_2^- + (\Xi^- K_2^-) K_1^+ + \Xi^- (K_1^+ K_2^-) + \Xi^- K_1^+ K_2^- \\
C_3^{(3)}\,(\Xi^- K_1^- K_2^+) &= (\Xi^- K_1^-) K_2^+ + (\Xi^- K_2^+) K_1^- + \Xi^- (K_1^- K_2^+) + \Xi^- K_1^- K_2^+ \\
C_4^{(3)}\,(\Xi^- K_1^- K_2^-) &= (\Xi^- K_1^-) K_2^- + (\Xi^- K_2^-) K_1^- + \Xi^- (K_1^- K_2^-) + \Xi^- K_1^- K_2^-
\end{aligned} \tag{3.6}$$

Later in this thesis, we will label the correlations according to the charges of the kaons with respect to the charge of the Ξ. As the charge of the Ξ is negative, we say that the charge of a K^+ is Opposite Sign (OS). For a K^-, it is Same Sign (SS). Correlations can then be referenced as follow: $(\Xi^- K_1^+ K_2^+)$ = OSOS, $(\Xi^- K_1^+ K_2^-)$ = OSSS, $(\Xi^- K_1^- K_2^+)$ = SSOS and $(\Xi^- K_1^- K_2^-)$ = SSSS.

The aim of the balance function is to get rid of everything except the $(\Xi^- K^+ K^+)$ triplet. In order to do so, we combine the correlations in eq. 3.6 using addition and subtraction. We make the assumption that the charge of an uncorrelated particle does not matter, and define the balance function as follows:

$$\begin{aligned}
BF &= C_1 - C_2 - C_3 + C_4 \\
&= OSOS - OSSS - SSOS + SSSS \\
&= (\Xi^- K_1^+ K_2^+) + \Xi^-(K_1^+ K_2^+) - \Xi^-(K_1^+ K_2^-) - \Xi^-(K_1^- K_2^+) + \Xi^-(K_1^- K_2^-) \\
&= (\Xi^- K_1^+ K_2^+) + Uncorrelated\ \ trigger
\end{aligned} \tag{3.7}$$

We are left with the $(\Xi^- K^+ K^+)$ triplet and the kaon correlations with an uncorrelated Ξ^-, that we will call the uncorrelated trigger.

3.3.4 Detector Acceptance Effect and Event Mixing

When plotting the correlation function in $\Delta\eta$, we have to get rid of a detector acceptance effect present in the result. As discussed in section 2.2.1, the detector acceptance is limited in $|\eta|$, causing the correlation distributions to be convoluted with the detector acceptance [29]. In order to remove this detector acceptance effect, we will do the correlation functions for particles in different events. With particles coming from different events, the correlation does not have physical meaning as there should not be any physics correlation between independent collisions, therefore the result we will obtain is only due to the detector acceptance. We obtain this plot by mixing the Ξ from one event, the first kaon from a previous event and the second kaon from another previous event. To obtain a satisfying result, we have to ensure the three different events are similar. In this study, we will mix events according to their multiplicity. Our same-event correlation is then divided by the acceptance correction, which has been normalised to 1 as shown in figure 3.4.

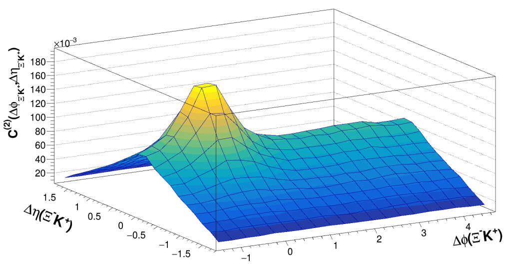

(a) Raw result for the $(\Xi^- K^+)$ correlation

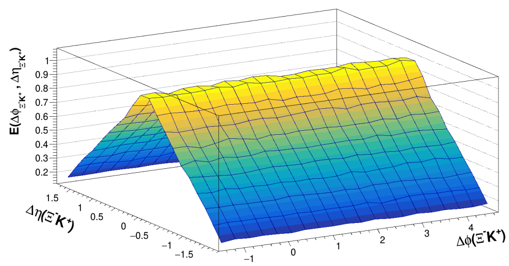

(b) Detector acceptance for the $(\Xi^- K^+)$ correlation

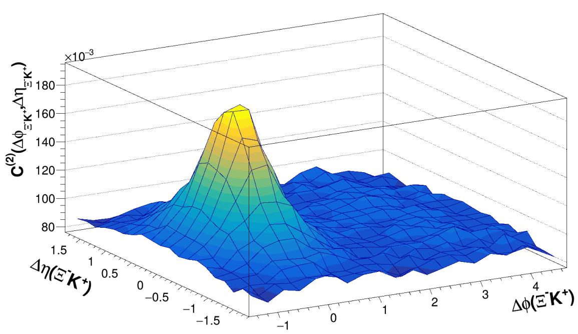

(c) Final result for the $(\Xi^- K^+)$ correlation

Figure 3.4: Two particle correlations correction method

To remove the uncorrelated trigger terms discussed above in section 3.3.3 from our balance function, we will operate in a similar way by doing a mixed event correlation. However, we showed in equation 3.7 that the uncorrelated trigger was the result of a correlation only between kaons. We take the Ξ from one event, and the kaon pair from a previous event. The mixing is once again multiplicity-depend. In order to ensure this condition, we create pools for different ranges of the multiplicity, and fill them with a determined number of events with similar multiplicity. We then do the correlation between the Ξ of a new event and the kaons of all events is the corresponding pool. Once this is done, we replace the oldest event in the pool by the newest one, and repeat this operation for the whole data set. The obtained correlation functions will then be subtracted from our three particle correlation function, for both $\Delta\phi$ and $\Delta\eta$. Therefore, our corrected correlation function is obtained as:

$$C^{(3)}(\Delta\phi, \Delta\eta) = \frac{S(\Delta\phi, \Delta\eta)}{E(\Delta\phi, \Delta\eta)} - \frac{M(\Delta\phi, \Delta\eta)}{E(\Delta\phi, \Delta\eta)} \tag{3.8}$$

where S$(\Delta\phi, \Delta\eta)$ corresponds to the same event results, M$(\Delta\phi, \Delta\eta)$ to the mixed event results and E$(\Delta\phi, \Delta\eta)$ to the detector acceptance effect. Those labels are used in sections 4.1.2 and 4.2.2 to differentiate the distributions between same event correlations and mixed event correlations. The BFs presented in sections 4.1.3 and 4.2.3 have subscripts **S** and **M** for the same event BF and the mixed event BF respectively. The Final Balance Function will then be referred to as $\mathbf{BF}_F$, such that BF$_F$ = BF$_S$ - BF$_M$.

3.3.5 Multiplicity dependency

We will also present our results according to different multiplicity bins in order study the multiplicity dependency of the ($\Xi^- K^+ K^+$) correlation. By plotting the multiplicity of all events and the multiplicity of events with at least one Ξ^-, we notice that all events have a low number of entries for low multiplicity (see figure 3.5a). The number of events with a Ξ is rather small compare to the total number of events, but its multiplicity peak is broader (see figure 3.5b), meaning that events with at least one Ξ^- tend to produce more particles, raising the interest in looking at the BF accordingly to the multiplicity.

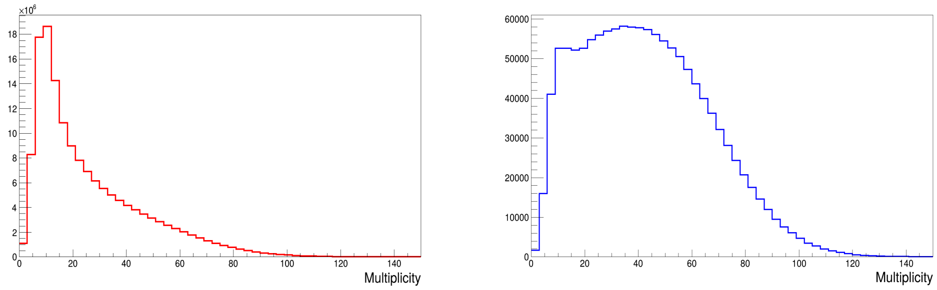

(a) All events (b) Events with at least one Ξ

Figure 3.5: Event multiplicity distribution for Monte-Carlo

Figure 3.6 presents the same quality assurance plots done in figure 3.5 but for the real data. However, the multiplicity from V0M (see section 2.2.1) is expressed in percentile, and a low percentile corresponds to a high-multiplicity. The multiplicity distribution is flat for all events, as shown in figure 3.6a, because of the percentile calibration. Events with at least one Ξ have high multiplicity, as evidenced by the peak at low multiplicity percentile shown in figure 3.6b.

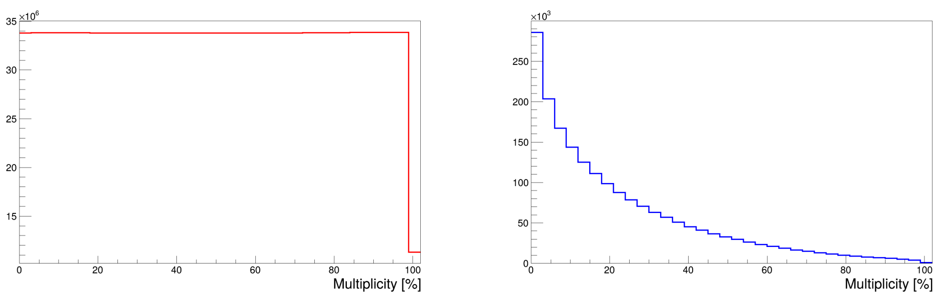

(a) All events (b) Events with at least one Ξ

Figure 3.6: Event multiplicity distribution in multiplicity percentile for real data

4 Results

Every correlation and balance function have been corrected for the detector acceptance 3.3.4. The mixed-events correlations used for this correction are shown in the Appendix, figures A1 to A4.

4.1 Monte-Carlo results

To begin our analysis on the production mechanisms of the $(\Xi^- K^+ K^+)$ triplet, two- and three-particle correlations were investigated in 300 million simulated p+p collision events, generated with PYTHIA.

4.1.1 Two-particle correlations

The two-particle correlation plot for $(\Xi^- K^+)$, defined in section 3.3.1, is shown in figure 3.4c. We observe a peak at $\Delta\phi = \Delta\eta = 0$, meaning that the Ξ^- and the K^+ are produced close to each other in angular-space. The two-particle correlation plot for $(\Xi^- K^-)$ is shown in figure 4.1. We still observe a peak at $\Delta\phi = \Delta\eta = 0$, but a ridge along $\Delta\phi = \pi$ induces that the kaon is produced mainly back-to-back with the Ξ^-.

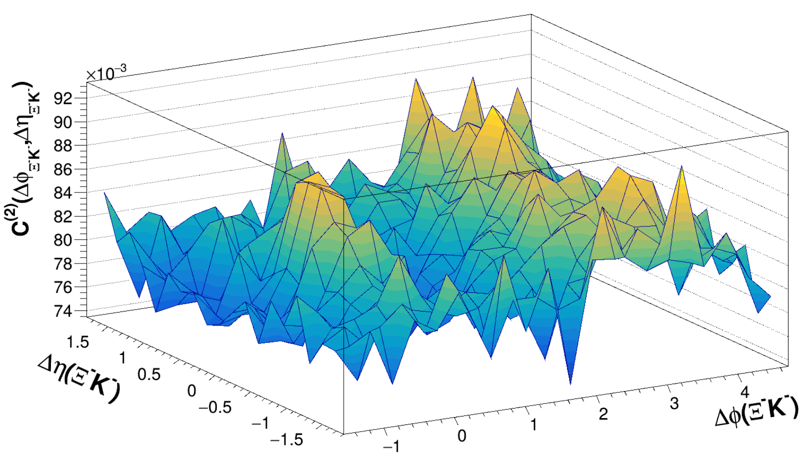

Figure 4.1: $(\Xi^- K^-)$ correlation in MC

The two-particle correlations of only the kaon pair $(K^\pm K^\pm)$, which results are presented in figure 4.2. In each distribution, regardless of the kaon charges, we observe a peak at $\Delta\phi = \Delta\eta = 0$, so the two kaons are once again produced close to each other in both pseudorapidity and azimuthal angle. But for the $+/+$ and $-/-$ distributions, hence when the two kaons have the same charge, we also observe a ridge along $\Delta\phi = \pi$. This would mean that for these two specific kaon charge combinations, kaons are also produced back-to-back to each other, with a non specific relative pseudorapidity value. Some production at $\Delta\phi = \pi$ is perceptible for the $+/-$ and the $-/+$ distributions, but it seems disfavoured compared to the previously discussed production mechanism. We also note that the size of the correlation function of the opposite kaon signs distributions is twice as large as the size of the correlation function of the same sign distributions.

Such results for the two-particle correlations were expected, due to various physics mechanisms, such as jet production. Indeed, back-to-back production is a way to balance the transverse momentum p_T in particle production.

These two-particle-correlations will appear in the three-particle correlations as well, and will be subtracted to reveal the true three-particle production process.

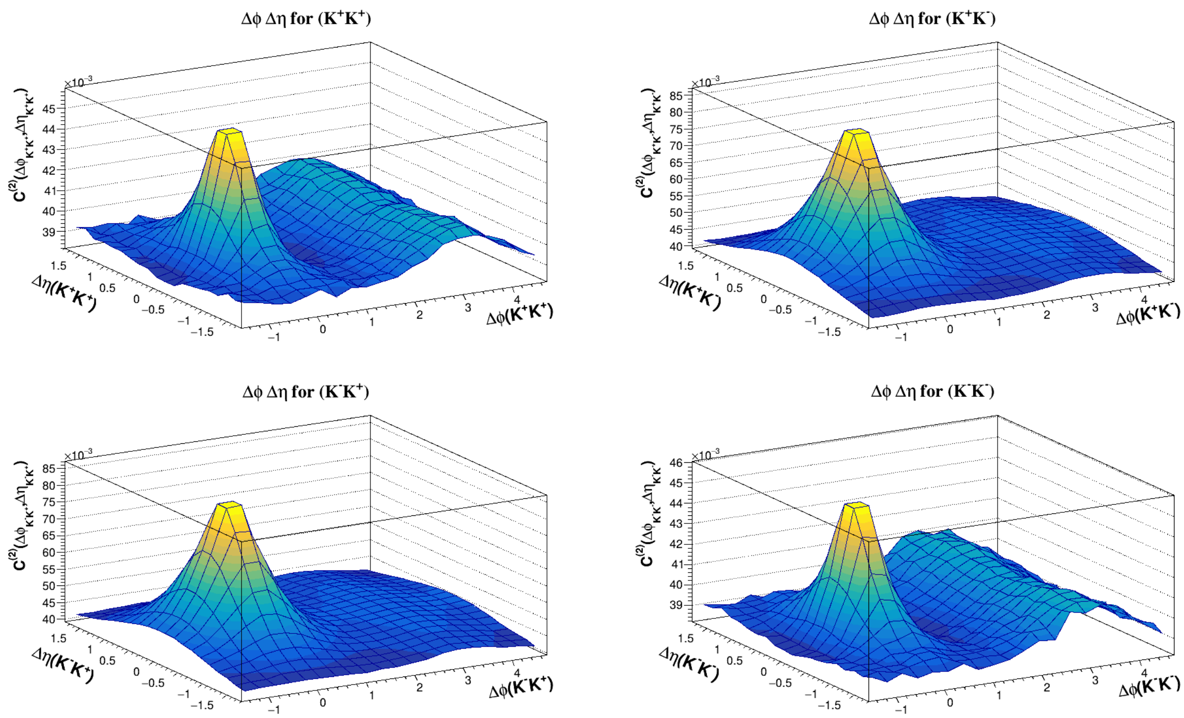

Figure 4.2: Two-particle correlation of kaon pairs for different kaon charge combinations in MC

4.1.2 Three particle correlations

The following distributions present in the z-axis the sizes of the correlations, defined in equation 3.4 and named with the method presented in section 3.3.4.

Figure 4.3 shows the three-particle (ΞKK) correlations for different combinations of kaon charges as a function of $\Delta\phi$, the difference in azimuthal angle. We observe the following

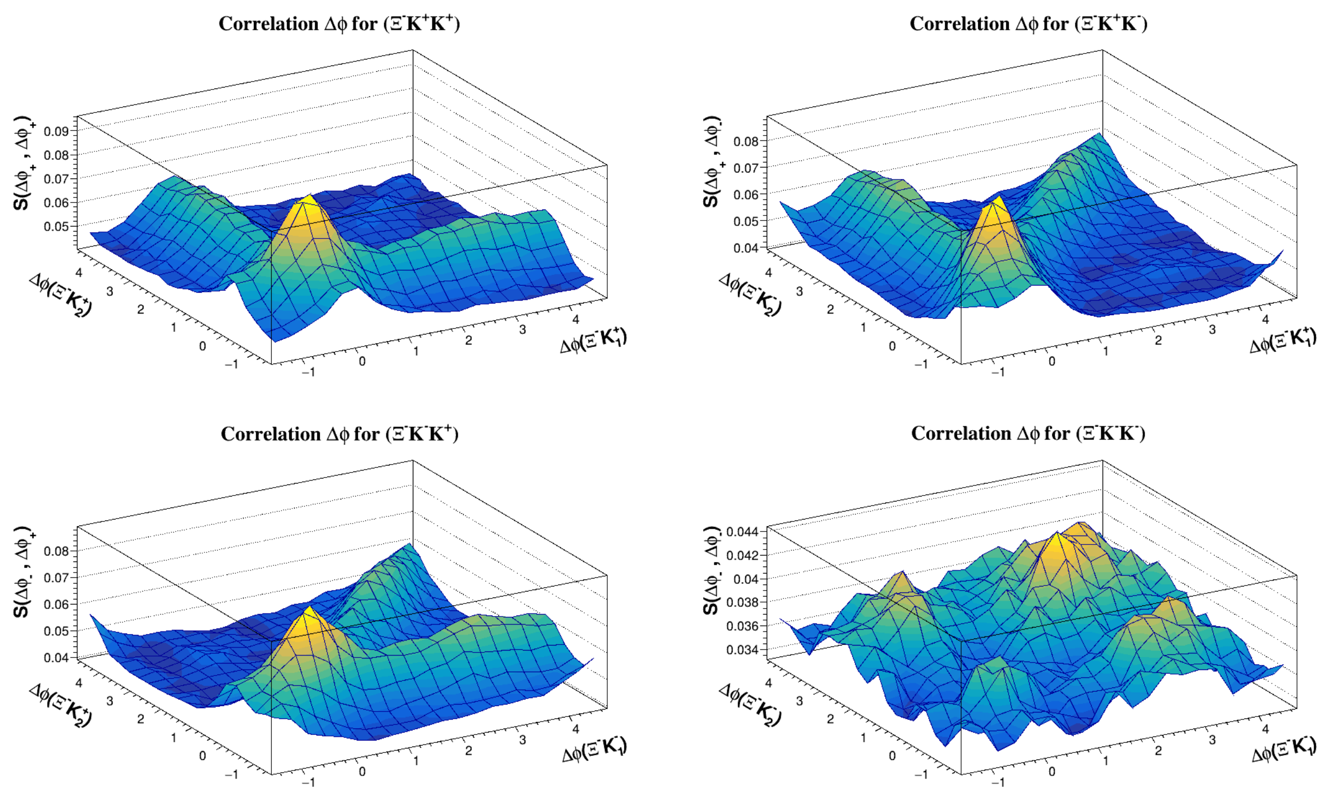

Figure 4.3: MC Correlations for $\Delta\phi$ for different combinations of kaon signs

features:

- $(\Xi^- K_1^+ K_2^+)$ or OSOS : We observe a peak at $\Delta\phi(\Xi^- K_1^+) = \Delta\phi(\Xi^- K_2^+) = 0$. This represents a production mechanism that favours all three particles created nearby. We also observe two ridges when the difference in azimuthal angle of one kaon is equal to 0 and the difference for the other is equal to π, which suggest that only one kaon is close to the baryon, when the other does not have a specific position in angular-space.

- $(\Xi^- K_1^+ K_2^-)$ or OSSS : The peak at $\Delta\phi(\Xi^- K_1^+) = \Delta\phi(\Xi^- K_2^-) = 0$ is once again present, encouraging the idea of particles being produced close to each other in azimuthal angle space. We can observe one ridge along $\Delta\phi(\Xi^- K_1^+) = 0$, suggesting that K^+ is close to the Ξ^- but not K^-, and a new ridge along $\Delta\phi(\Xi^- K_1^+) = \Delta\phi(\Xi^- K_2^-)$. This would suggest that kaons are produced close, and at an equal distance to the baryon.

- $(\Xi^- K_1^- K_2^+)$ or SSOS : The results of this correlation plot are symmetrical to the one obtained in figure (b). The peak is still present, as well as the ridge along $\Delta\phi(\Xi^- K_1^-)$

$= \Delta\phi(\Xi^- K_2^+)$. The other ridge is now along $\Delta\phi(\Xi^- K_2^+) = 0$.

- $(\Xi^- K_1^- K_2^-)$ or SSSS : The peak at $\Delta\phi(\Xi^- K_1^-) = \Delta\phi(\Xi^- K_2^-) = 0$ is now disfavoured against a peak at $\Delta\phi(\Xi^- K_1^-) = 0$ and $\Delta\phi(\Xi^- K_2^-) = \pi$, a peak at $\Delta\phi(\Xi^- K_1^-) = \pi$ and $\Delta\phi(\Xi^- K_2^-) = 0$ and a larger peak at $\Delta\phi(\Xi^- K_1^-) = \Delta\phi(\Xi^- K_2^-) = \pi$. This would suggest that for two negative kaons, the nearby production of all three particles is disfavoured, but the production of one kaon with the Ξ^- and the other back-to-back is more likely, with the production of the two kaons back-to-back to the baryon and at an equal distance from the Ξ^- is the favoured production mechanism.

To understand those results, we have to recall the expression of each kaon combination correlation from equation (3.6). We know that OSSS, SSOS and SSSS are dominated by two-particle correlations, and if we look at the analysis we did for the kaon-pair correlations of the $(\Xi^- K^\pm)$ in section 4.1.1, it becomes apparent that all the distributions in 4.3 are dominated by two-particle correlations, even the OSOS distribution. Indeed, the ridge along the diagonal $\Delta\phi(\Xi^- K^+) = \Delta\phi(\Xi^- K^-)$ in the OSSS and SSOS correlations comes from the $(K^+ K^-)$ and $(K^- K^+)$ correlations shown in figure 4.2, where we saw that the two kaons were produced close to each other. For the same distributions, the ridge along only one axis is linked to the $(\Xi^- K^+)$ correlation shown in figure 3.4c and the $(\Xi^- K^-)$ correlation shown in figure 4.1, where the kaon with opposite sign to the Ξ^- is produced close to the trigger particle, irrespective of the position of the kaon with the same sign. For the SSSS correlation, the $\Delta\phi(\Xi^- K_1^-) = \Delta\phi(\Xi^- K_2^-) = 0$ is less favoured than the other positions as back-to-back production was favoured in the $(\Xi^- K^-)$ correlation and present in the $(K^- K^-)$ kaon correlation. Finally, for the OSOS correlation, the main correlations are due to two particle $(\Xi^- K^+)$ correlations (hence the ridges along each axis), which are mimicked by the OSSS and SSOS correlations, as well as a small contribution from the uncorrelated trigger combinations ($(K^+ K^-)$ correlations).

Figure 4.4 shows the three-particle $(\Xi K K)$ correlations for different combinations of kaon charges as a function of $\Delta\eta$, the difference in pseudorapidity. The detector effect correction has already been applied as mentioned in section 3.3.4. The peaks surrounding the edges are caused by statistical fluctuations as we are probing the limits of the pseudorapidity range

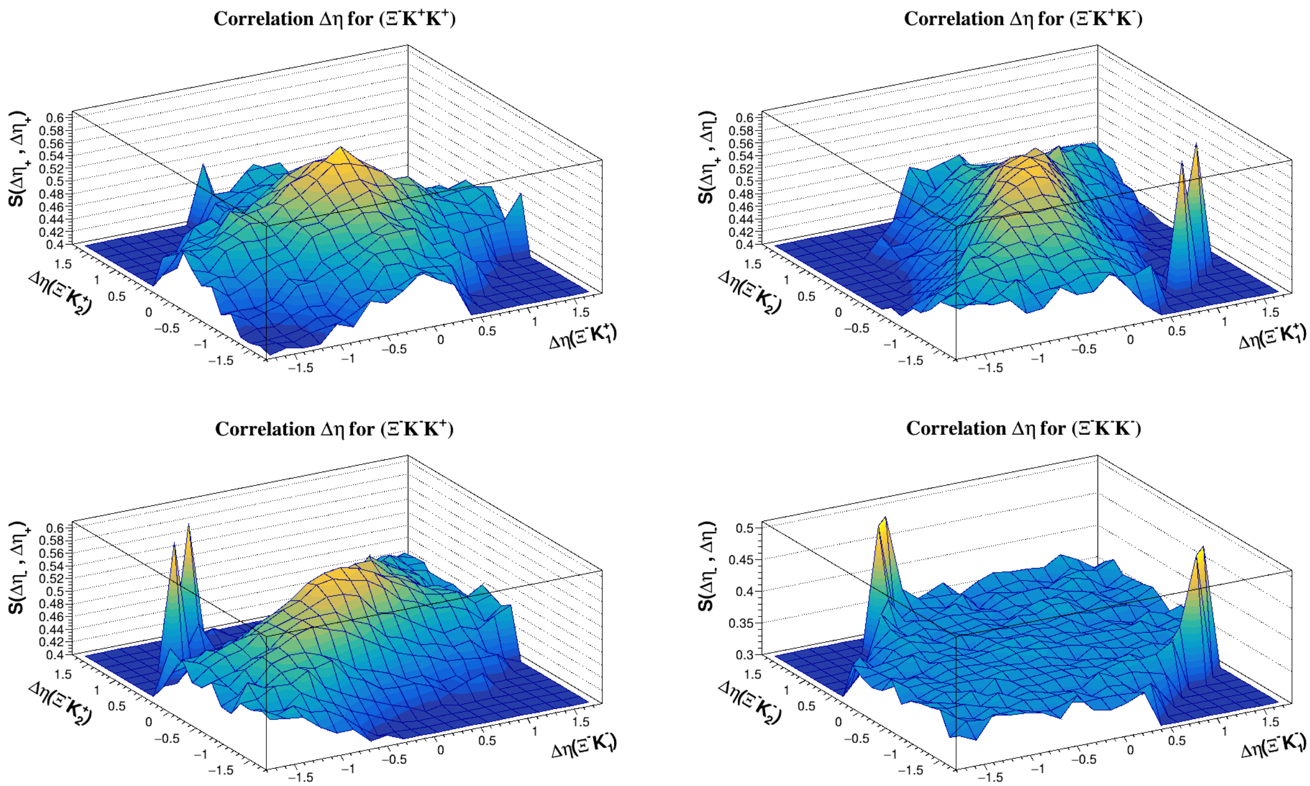

Figure 4.4: MC Correlations for $\Delta\eta$ for different combinations of kaon signs

for the detector (section 2.2). The z-axis ranges for the distributions have also been cut to observe the correlations, as the region past the edges is empty.

- $(\Xi^- K_1^+ K_2^+)$ or OSOS : The distribution has a small broad peak at $\Delta\eta(\Xi^- K_1^+) = \Delta\eta(\Xi^- K_2^+) = 0$, which means the three particles are produced close to each other.

- $(\Xi^- K_1^+ K_2^-)$ or OSSS : The peak at $\Delta\eta(\Xi^- K_1^+) = \Delta\eta(\Xi^- K_2^+) = 0$ is more prevalent, but a diagonal for $\Delta\eta(\Xi^- K_1^+) = \Delta\eta(\Xi^- K_2^-)$ also appeared. A ridge along $\Delta\eta(\Xi^- K_1^+)$ is visible, meaning that a production mechanism is favoured when the positive kaon is close to the Ξ^-, where the position of the second kaon does not matter, except the two previous discussed positions.

- $(\Xi^- K_1^- K_2^+)$ or SSOS : Symmetrically to the OSSS correlation, the ridge along the positive kaon axis is now on the y-axis, confirming that the positive kaon is close to the baryon.

- $(\Xi^- K_1^- K_2^-)$ or SSSS : A small ridge can be observed in the region where $\Delta\eta(\Xi^- K_1^- +)$ and $\Delta\eta(\Xi^- K_2^-) < 0$.

The two ridges in the OSSS and SSSS correlations can once again be explained by the kaon correlations and the two-particle correlations in figures 3.4c and 4.1: we know that the two kaons are at the same distance to each other in pseudorapidity, and that no position in relative pseudorapidity to the Ξ^- is favoured for the negative kaon. The same analysis applies to the SSSS distribution, without a positive kaon correlation to balance this absence of favoured position. Finally, the peak at $\Delta\eta(\Xi^- K_1^+) = \Delta\eta(\Xi^- K_2^+) = 0$ in the OSOS correlation matches the two-particle correlations, as it was the favoured pseudorapidity value for particle production in figure 3.4c.

The correlations in figures 4.3 and 4.4 motivated once again the need to get rid of the uncorrelated triggers, as shown in expression 3.7. Figure 4.5 shows the uncorrelated triggers distributions for $\Delta\phi$, the difference in azimuthal angle, obtained with event mixing as discussed in section 3.3.4.

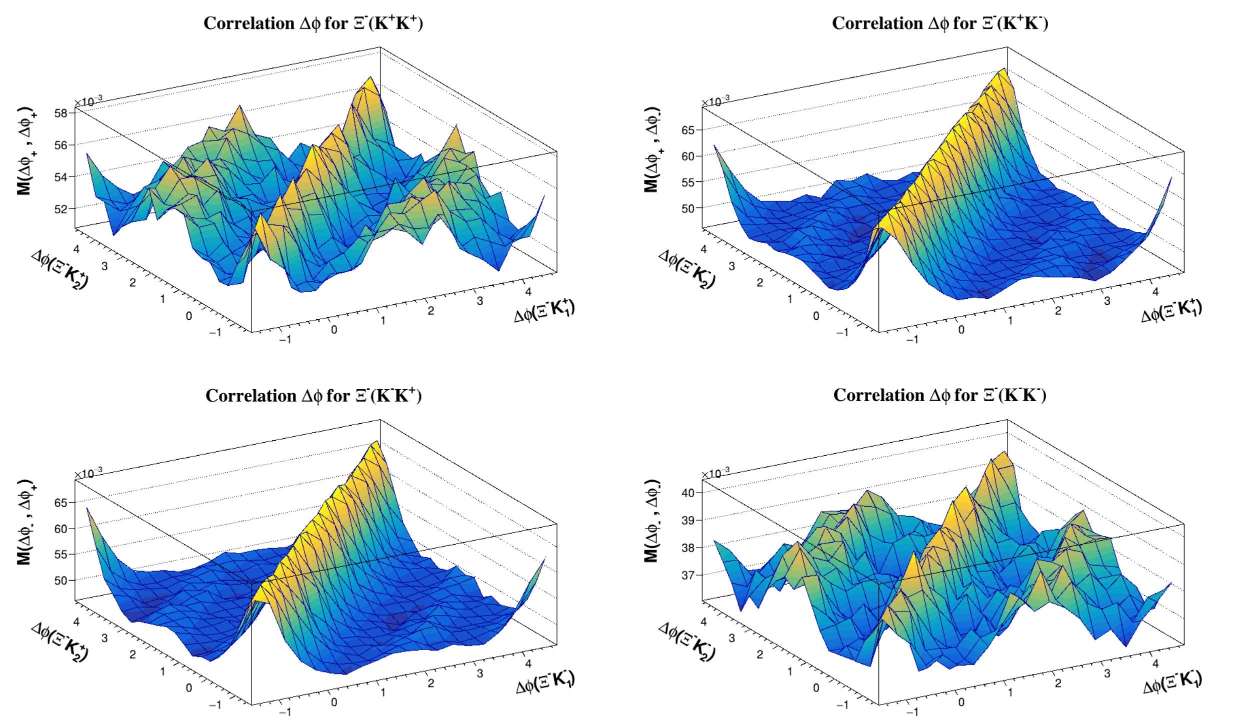

Figure 4.5: Mixed events Kaon Correlations for $\Delta\phi$ for different combinations of kaon signs

The OSOS and SSSS distributions have a "wave" behaviour, with three visible ridges. The most prominent one is located at $\Delta\phi(\Xi^- K_1^\pm) = \Delta\phi(\Xi^- K_2^\pm)$. The two other ones are located with a π shift between the two axis values (for instance $\Delta\phi(\Xi^- K_1^\pm) = 0$ and $\Delta\phi(\Xi^- K_2^\pm) = \pi$). As the Ξ^- is uncorrelated (originating from a different event), we can determine that the two kaons are produced both close to each other and back-to-back, which matches the two-particle correlations we presented in figure 4.2.

The OSSS and SSOS distributions have one singular ridge at $\Delta\phi(\Xi^- K_1^\pm) = \Delta\phi(\Xi^- K_2^\mp)$, once again matching the results in figure 4.2, where only one peak was present, hence meaning that the two kaons are produced next to each other.

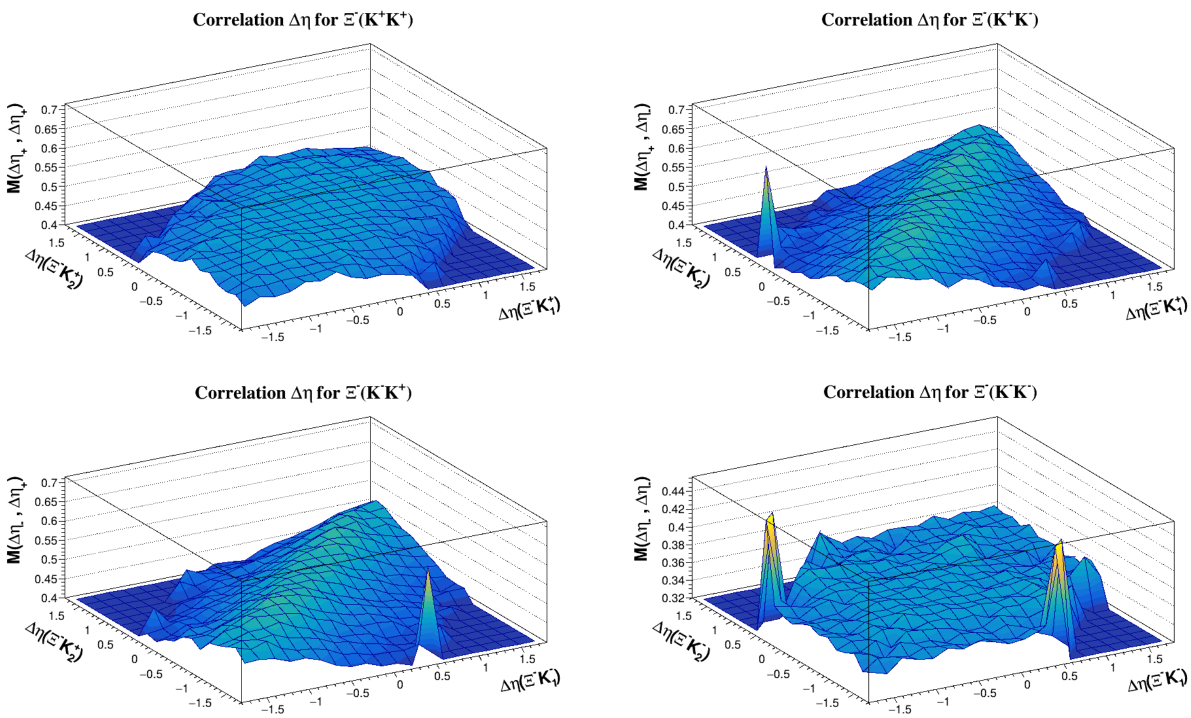

Figure 4.6: Mixed events Kaon Correlations for $\Delta\eta$ for different combinations of kaon signs

Figure 4.6 shows the uncorrelated triggers distributions for $\Delta\eta$, the difference in pseudorapidity, from equation (3.7), obtained as the results from figure 4.5.

The OSOS and SSSS $\Delta\eta$ event mixing correlations do not appear to have any specific peaks (excluding the ones on the range extremities that are caused by the detector correction and some fluctuations). Therefore, for those two kaon combinations, no position in pseudorapidity seems to be favoured, which matches the results in figure 4.2 where the ridge along $\Delta\phi(K^+K^+) = \pi$ and $\Delta\phi(K^-K^-) = \pi$ covered the whole difference in pseudorapidity range.

The main difference between the $(\Xi^- K^+ K^+)$ correlation in figure 4.3 is the absence of a peak around 0, explained by the fact that the Ξ^- is here uncorrelated, which prevents the peak from figure 3.4c to appear. For the OSSS and SSOS distributions, we note a ridge along $\Delta\eta(\Xi^- K^\pm) = \Delta\eta(\Xi^- K^\mp)$. It means that the two kaons are close to each other in pseudorapidity, which once again matches the results from figure 4.2, where the peak at $\Delta\phi(K^\pm K^\mp) = \Delta\eta(K^\pm K^\mp) = 0$ meant that the two kaons are close to each other.

4.1.3 Balance Functions

The results in figure 4.7 present the raw balance functions for $(\Xi^- K^+ K^+)$, OSOS - OSSS - SSOS + SSSS, hence without removing the uncorrelated triggers from figures 4.5 and 4.6. We can observe for the $\Delta\phi$ balance function a negative ridge in $\Delta\phi(\Xi^- K_1^+) = \Delta\phi(\Xi^- K_2^+)$, with two downwards peaks at $\Delta\phi(\Xi^- K_1^+) = \Delta\phi(\Xi^- K_2^+) = 0$ and $\Delta\phi(\Xi^- K_1^+) = \Delta\phi(\Xi^- K_2^+) = \pi$. A negative ridge is also visible in the $\Delta\eta$ balance function, centred at $\Delta\eta(\Xi^- K_1^+) = \Delta\eta(\Xi^- K_2^+)$. A certain number of peaks, both negative and positive, are also present in the $\Delta\eta$ distribution. Our understanding is that they originate from statistical fluctuations and are not actual $\Delta\eta$ values for which the strange flavoured particles are formed.

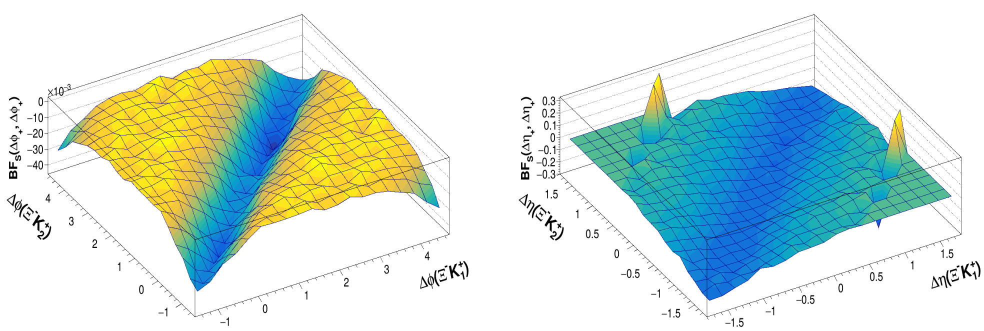

(a) Raw $\Delta\phi$ Balance Function (b) Raw $\Delta\eta$ Balance Function

Figure 4.7: Raw Balance Functions for $(\Xi^- K^+ K^+)$

As stated above, the BFs in figure 4.7 do not yet present the structure of the true three-particle interactions, as the uncorrelated kaon pairs are still included in this result, and as we saw in section 4.2.2, they are the main contributors to the correlations observed.

The mixed events balance functions are presented in figure 4.8. We can observe that for

$\Delta\phi$, the ridge in $\Delta\phi(\Xi^- K_1^+) = \Delta\phi(\Xi^- K_2^+)$ is also present but this time is really smooth, with no significant peak appearing on the distribution. Similarly for $\Delta\eta$, the mixed event balance function is similar to the raw balance function (see figure 4.8b), without surrounding peaks around the $\Delta\eta$ range. Again, from the very similar shape of the BF in figure 4.7 and 4.8 we can conclude that the initial correlations results were mainly uncorrelated triggers. The results in figures 4.9a and 4.9b present our final BFs, obtained by subtracting the results in figures 4.8 from the ones in figure 4.7.

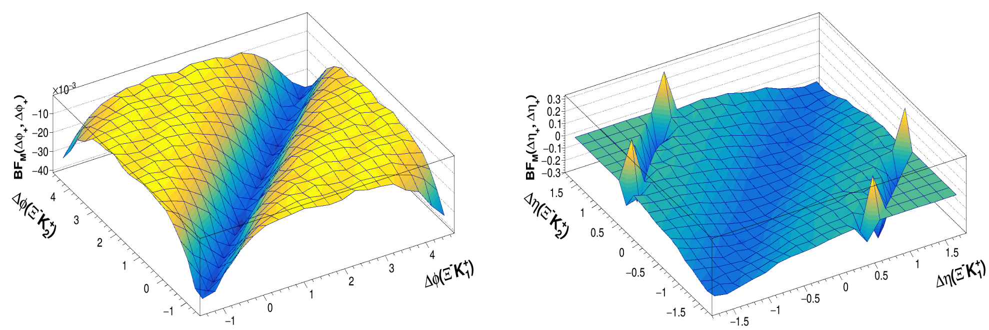

(a) Mixed Events $\Delta\phi$ Balance Function (b) Mixed events $\Delta\eta$ Balance Function

Figure 4.8: Uncorrelated triggers balance functions for $(\Xi^- K^+ K^+)$

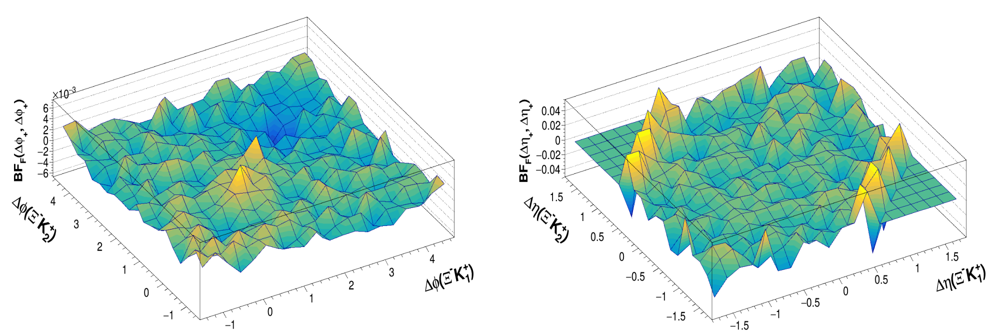

(a) Final $\Delta\phi$ Balance Function for $(\Xi^- K^+ K^+)$ (b) Final $\Delta\eta$ Balance Function for $(\Xi^- K^+ K^+)$

Figure 4.9: Final Balance Functions for $(\Xi^- K^+ K^+)$

For $\Delta\phi$, we observe that the ridge has disappeared, but two negative peaks are still present in $\Delta\phi(\Xi^- K_1^+) = \Delta\phi(\Xi^- K_2^+) = 0$ and $\Delta\phi(\Xi^- K_1^+) = \Delta\phi(\Xi^- K_2^+) = \pi$, with the second one being far more important. We also observe a small peak right after $\Delta\phi(\Xi^- K_1^+) = \Delta\phi(\Xi^- K_2^+)$

= 0. On the other hand, except the surrounding peaks, the $\Delta\eta$ distribution is rather flat, meaning that no precise value for the pseudorapidity is favoured.

An important observation is that the three-particle ($\Xi^- K^+ K^+$) BF is very small in comparison to the two-particle ($\Xi^- K^+$) correlation function. It means that the Ξ^- is often balanced by one K^+, but very rarely balanced by two K^+ mesons.

We performed a few quality assurance plots by computing the BF for a specific range of the multiplicity (figures 4.10 and 4.11). For the $\Delta\phi$ BFs, the main regions of interest are located along $\Delta\phi(\Xi^- K_1^+) = \Delta\phi(\Xi^- K_2^+)$, meaning that what we observe might still be caused by some uncorrelated triggers. For the the two lowest multiplicity ranges, we see two negative peaks at $\Delta\phi(\Xi^- K_1^+) = \Delta\phi(\Xi^- K_2^+) = 0$ and $\Delta\phi(\Xi^- K_1^+) = \Delta\phi(\Xi^- K_2^+) = \pi$, and some peaks in the region in between. As the multiplicity increases, the negative peaks seem to be less pronounced in favour of a flatter distribution. For the $\Delta\eta$ BF, we observe a peak around at $\Delta\eta(\Xi^- K_1^+) = \Delta\eta(\Xi^- K_2^+) = 0$ regardless of the multiplicity, meaning that the favoured production mechanism is for all particles close in to each other in pseudorapidity space. A lot of variation is observable in every distribution, caused partly by the detector acceptance removal that forces us to divide by low values.

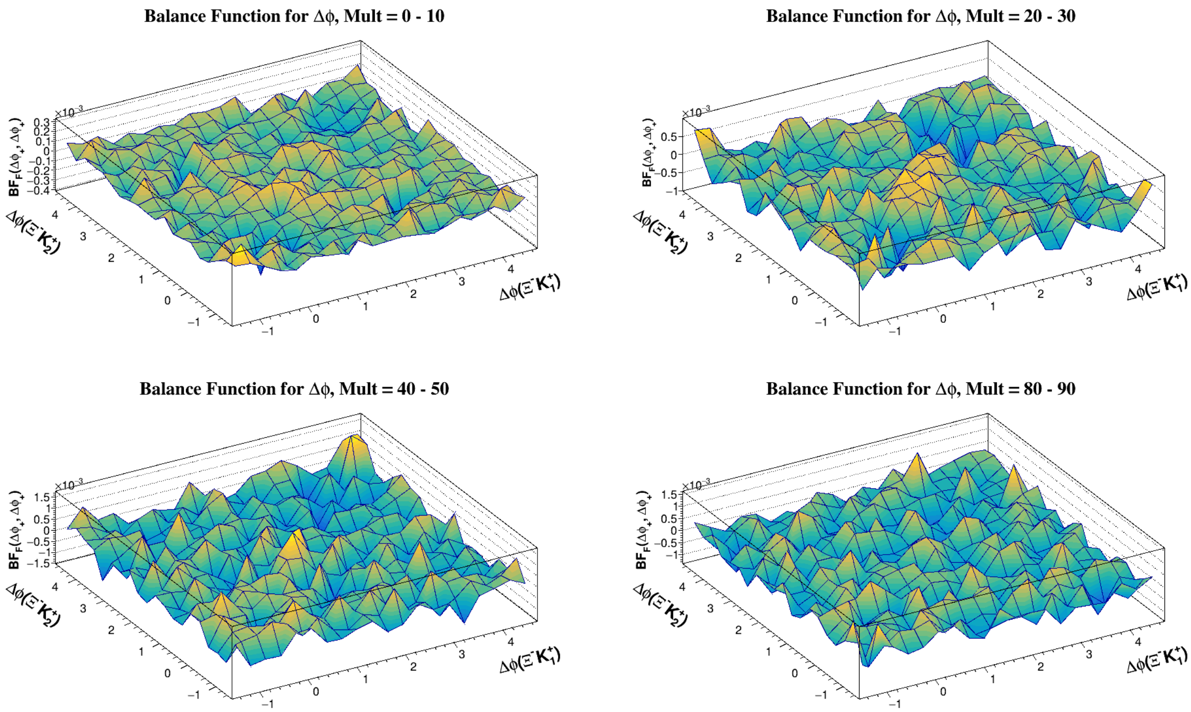

Figure 4.10: Corrected Balance Functions for $\Delta\phi$ different ranges of multiplicity

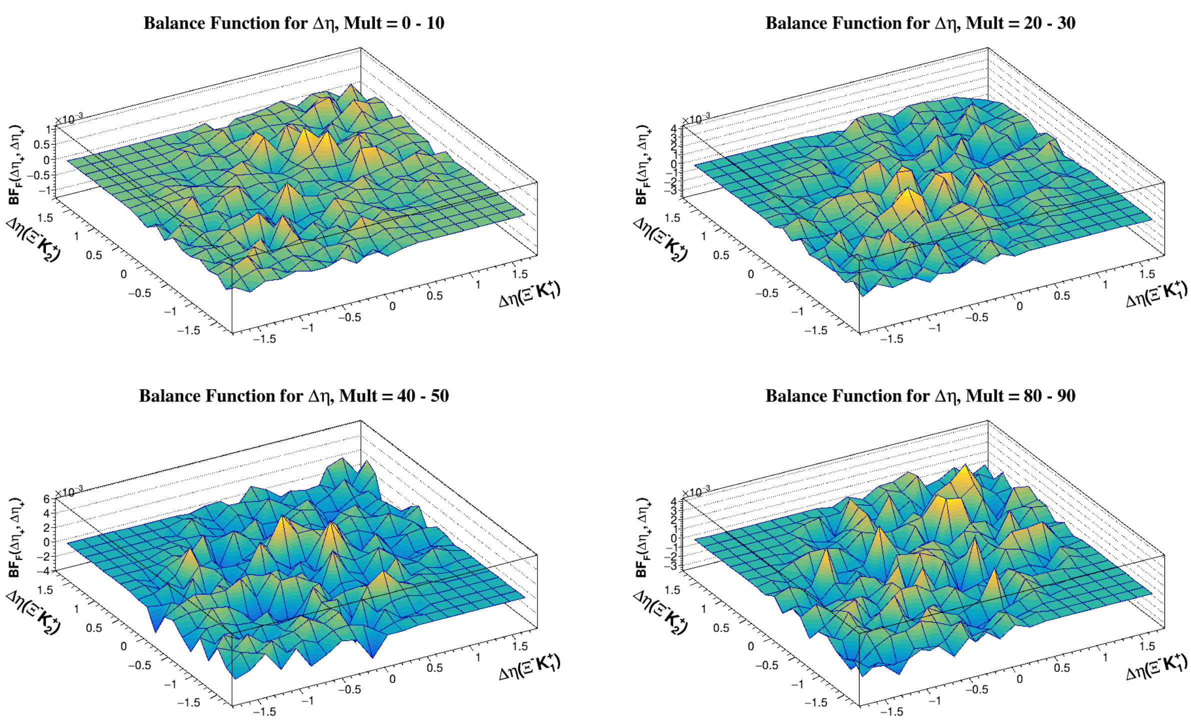

Figure 4.11: Corrected Balance Functions for $\Delta\eta$ different ranges of multiplicity

4.1.4 Biased generation

For the ROOT files generated using the method discussed in section 3.1.1, we obtain the distributions in figure 4.12. We observe that unlike the final balance functions obtained for the unbiased MC generated events, we have for the $\Delta\phi$ correlation a single peak at $\Delta\phi(\Xi^- K_1^+)$ $= \Delta\phi(\Xi^- K_2^+) = 0$. We can also observe a small ridge around $\Delta\phi(\Xi^- K_1^+) = \Delta\phi(\Xi^- K_2^+) =$ π, with the assumption it is caused by remnants of the particles formed on the string. For the $\Delta\eta$ correlation, we observe a peak centred at $\Delta\eta(\Xi^- K_1^+) = \Delta\eta(\Xi^- K_2^+) = 0$, unlike the relatively flat distribution observed with the previous MC simulation. According to those results, the $(\Xi^- K^+ K^+)$ triplet production is extremely favoured simultaneously, and can barely happen back-to-back.

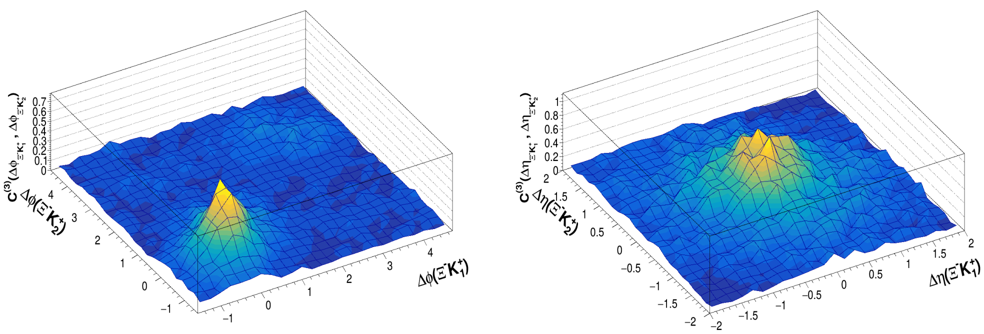

(a) $(\Xi^- K^+ K^+)$ Correlation for $\Delta\phi$ (b) $(\Xi^- K^+ K^+)$ Correlation for $\Delta\eta$

Figure 4.12: Correlations for biased event generation

The result obtained in figure 4.12 is similar to our result for $(\Xi^- K^+ K^+)$ if the ridges along the axes were suppressed for the $\Delta\phi$ correlation. We know that those ridges are caused by the uncorrelated triggers, therefore we can conclude that the mixing performed in 4.5 has to be improved.

4.2 Real data results

The three-particle correlations were measured in data from p-p collisions at $\sqrt{s} = 13$ TeV collected by the ALICE experiment in 2017 and 2018, comprising 1.1 billion events.

4.2.1 Two-particle correlations

The same investigation of two-particle correlation has been performed for the real data samples. The results are provided in figures 4.13 and 4.14. We observe a significant amount of statistical fluctuations on figures 4.13a and 4.13b, but the shapes of the correlations match what was observed in section 4.1.1: the Ξ^- and the K^+ are produced close to each other in both azimuthal angle and pseudorapidity, whereas the Ξ^- and the K^- are mainly produced back-to-back. The kaon correlations in figure 4.14 have the same shape as the MC results in figure 4.2.

We also note that the $K+$ and the K^- are roughly equally likely to be produced back-to back with the Ξ^- in figures 4.13 and 4.14, with same size if we look at the z-axes. SS correlations ((Ξ^-K^-) and (K^+K^+) and (K^-K^-)) then show momentum conservation in jet production, while the OS correlations ((Ξ^-K^+) and (K^+K^-) show additional production close in momentum space.

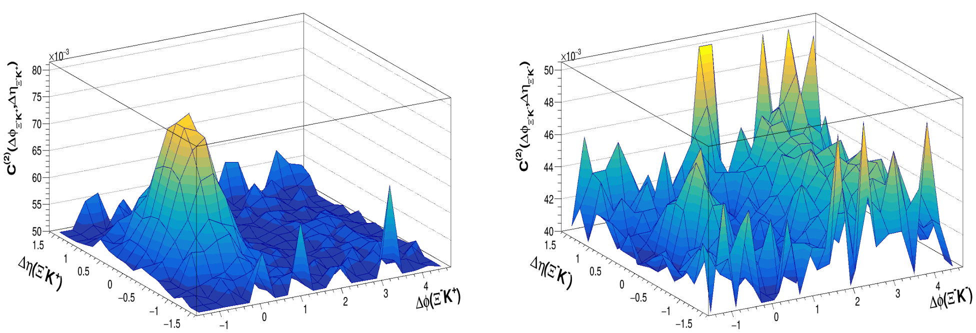

(a) (Ξ^-K^+) correlation

(b) (Ξ^-K^-) correlation

Figure 4.13: Two-particle correlations for (Ξ^-K)

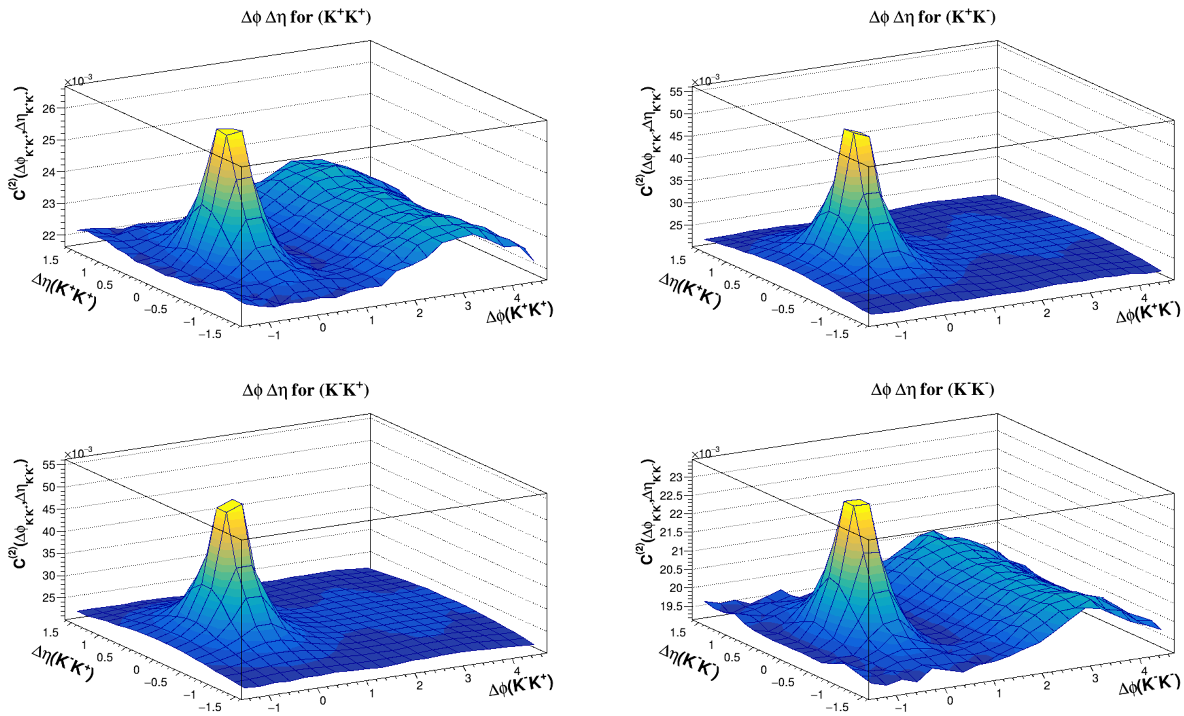

Figure 4.14: Two-particle correlations of the Kaon pair for different kaon charges

4.2.2 Three particle correlations

Figure 4.15 shows the different correlations for same event particles. The main features of the histograms are similar to the histograms in figure 4.3:

- $(\Xi^- K_1^+ K_2^+)$ or OSOS : We observe a peak at $\Delta\phi(\Xi^- K_1^+) = \Delta\phi(\Xi^- K_2^+) = 0$, which lets us conclude that nearby particle production is favoured. The two ridges along $\Delta\phi(\Xi^- K^+) = 0$ are present as in figure 4.3, with two peaks where the difference in azimuthal angle with the other kaon is equal to π. It means that one kaon can be produced close to the Ξ^-, whereas the other kaon will be produced back-to-back to the baryon.

- $(\Xi^- K_1^+ K_2^-)$ or OSSS : The peak at $\Delta\phi(\Xi^- K_1^+) = \Delta\phi(\Xi^- K_2^-) = 0$ is once again present, enforcing the idea of particle production close in phase-space being favoured. We observe that unlike the same correlation in figure 4.3, the ridge along $\Delta\phi(\Xi^- K_1^+) = 0$ is significantly smaller compared to the ridge along $\Delta\phi(\Xi^- K_1^+) = \Delta\phi(\Xi^- K_2^-)$. This would suggest that kaons are mainly produced at an equal distance from the Ξ^-.

- $(\Xi^- K_1^- K_2^+)$ or SSOS : The results of this correlation plot are symmetrical to the one obtained in figure (b). The peak is still present, as well as the ridge along $\Delta\phi(\Xi^- K_1^-)$ $= \Delta\phi(\Xi^- K_2^+)$. The other ridge is now along $\Delta\phi(\Xi^- K_2^+) = 0$, and is also significantly smaller compared to the diagonal ridge.

- $(\Xi^- K_1^- K_2^-)$ or SSSS : This histogram is similar to the SSSS Monte-Carlo correlation in figure 4.3, with a peak at $\Delta\phi(\Xi^- K_1^-) = \Delta\phi(\Xi^- K_2^-) = \pi$, two smaller peaks at $\Delta\phi(\Xi^- K_1^-) = \pi$ with $\Delta\phi(\Xi^- K_2^-) = 0$ and $\Delta\phi(\Xi^- K_1^+) = 0$ with $\Delta\phi(\Xi^- K_2^+) = \pi$, and finally a smaller peak at $\Delta\phi(\Xi^- K_1^-) = \Delta\phi(\Xi^- K_2^-) = 0$. Therefore the production of the two kaons back-to-back to the baryon and close to each other seems to be favoured, although the SSSS correlation is significantly smaller that the other three charge combinations.

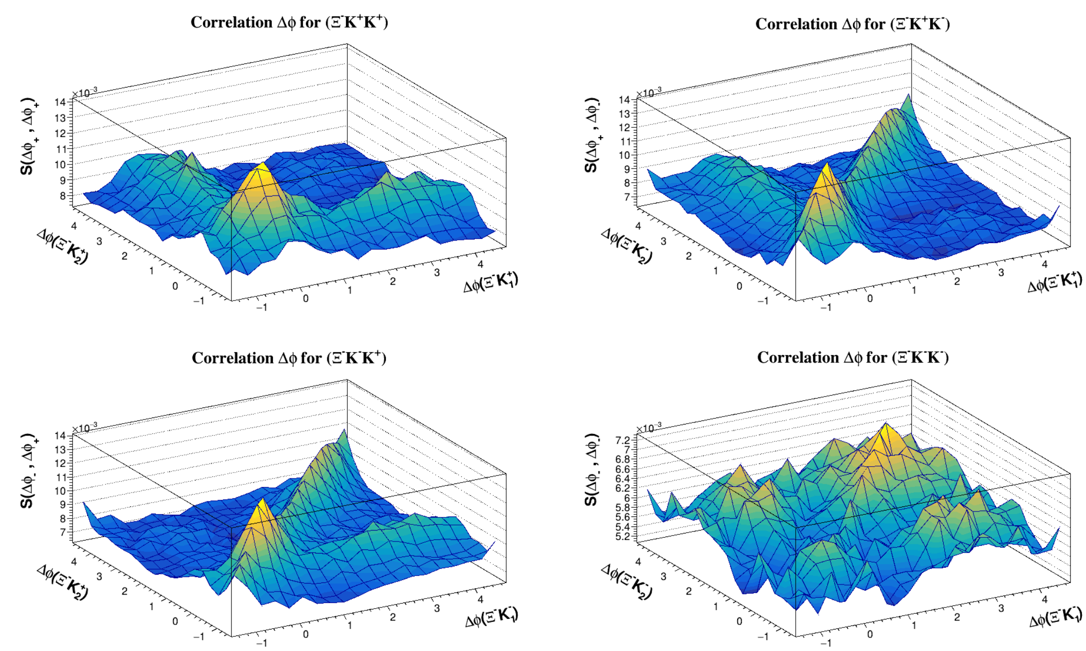

Figure 4.15: Real data Correlations for $\Delta\phi$ for different combinations of kaon signs

The results obtained for the $\Delta\eta$ correlations with the real data are shown in figure 4.16. The OSOS correlation presents a peak around $\Delta\eta(\Xi^- K_1^+) = \Delta\eta(\Xi^- K_2^+) = 0$, meaning that the three particles are produced close to each other. The OSSS and the SSOS distribution present a ridge along $\Delta\eta(\Xi^- K_1^+) = \Delta\eta(\Xi^- K_2^+)$, with a peak centred at 0. Therefore, the two opposite sign kaons are at a similar distance to the Ξ^-. Finally, the SSSS correlation does not present a favoured pseudorapidity value for particle production. The real data results for $\Delta\eta$ correlations, like the $\Delta\phi$ correlations, are close to the MC results discussed in section 4.1.2.

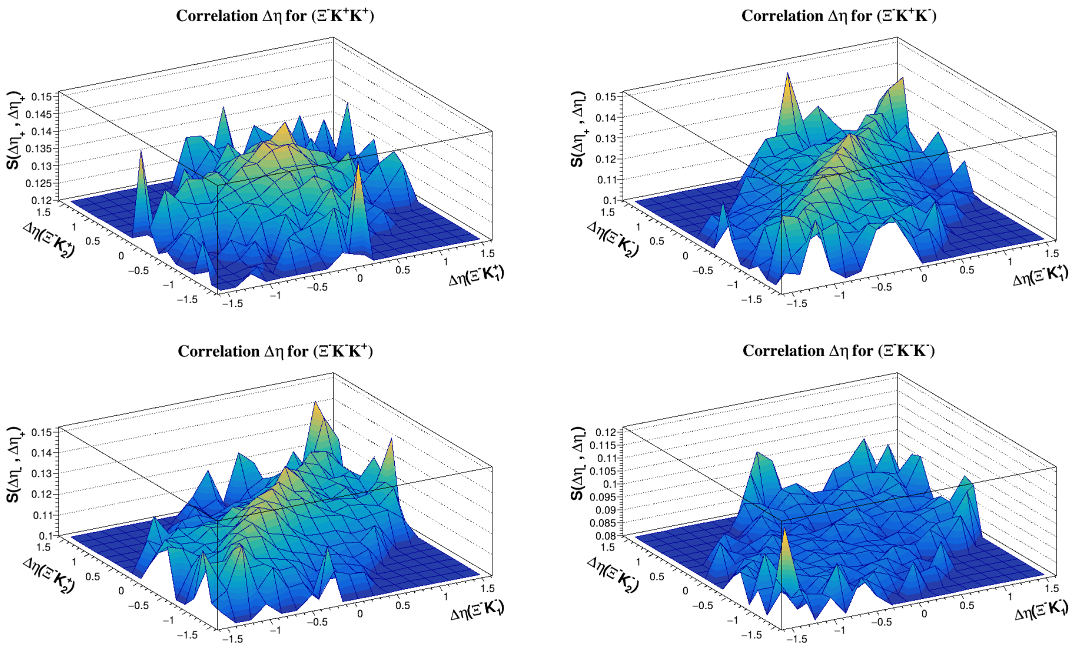

Figure 4.16: Real data Correlations for $\Delta\eta$ for different combinations of kaon signs

The obtained correlations, either for $\Delta\phi$ or $\Delta\eta$, can be explained using the expressions in (3.6) and the two-particle correlations from 4.2.1. The distributions are dominated by the uncorrelated triggers, raising once again the need for event mixing.

Figure 4.17 shows the correlation functions of the uncorrelated triggers (or kaon pairs). The results presented in figure 4.17 are similar to the ones in 4.5. The same analysis regarding the results obtained in figure 4.14 can be done, we however note that for the OSOS correlation and SSSS correlation, we observe more statistical fluctuations.

Similarly to the mixed events correlation analysis done in section 4.1, the results presented in figure 4.18 agree with the results in figure 4.14. Indeed, no specific pseudorapidity value seems to be favoured for the OSOS and the SSSS correlations, whereas values such that $\Delta\eta(\Xi^-K^\pm) = \Delta\eta(\Xi^-K^\mp)$ favour a production mechanism where kaons are close to each other, such as the $(K^\pm K^\mp)$ presented in figure 4.14.

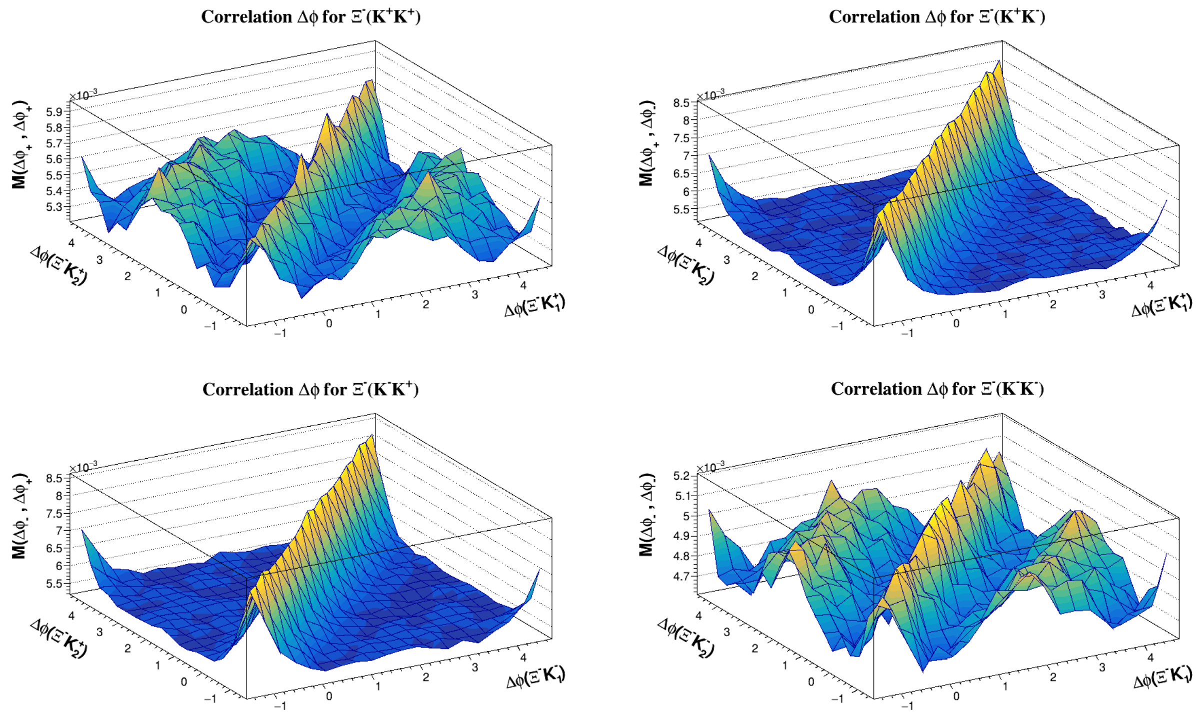

Figure 4.17: Mixed events Kaon Correlations for $\Delta\phi$ for different combinations of kaon signs

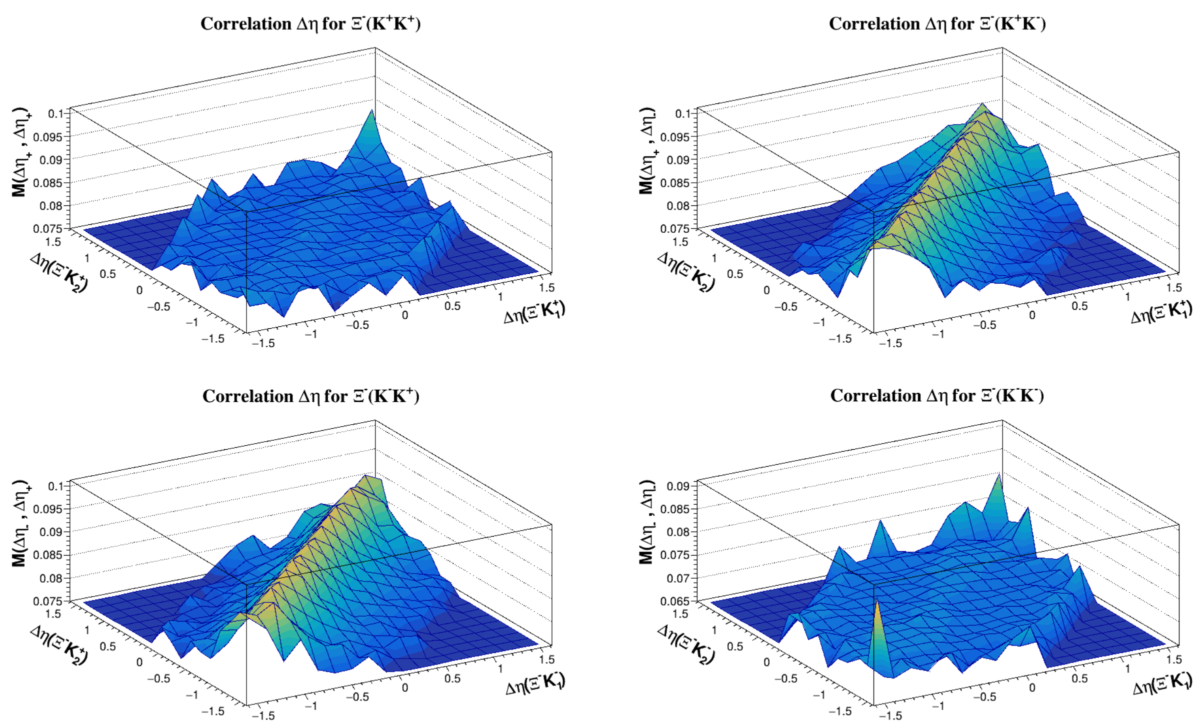

Figure 4.18: Mixed events Kaon Correlations for $\Delta\eta$ for different combinations of kaon signs

The results shown in figures 4.15 to 4.18 had "fake Ξ^-" correlations subtracted as described in section 3.2.1, with the values presented in table 3.II. The shape of the fake Ξ candidates correlations are shown in the Appendix, figure A5.

4.2.3 Balance Functions

The raw balance functions presented in figure 4.19 are similar to the simulated events results in figure 4.7. We still notice a centred negative ridge both for the $\Delta\phi$ and $\Delta\eta$ distribution.

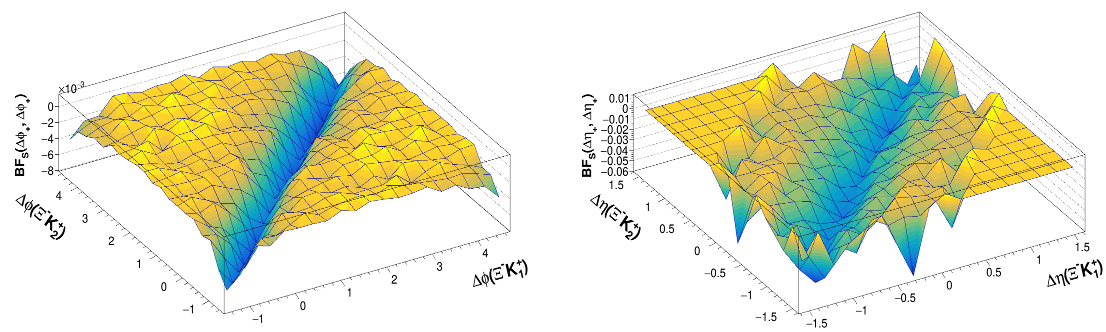

(a) Raw $\Delta\phi$ Balance Function

(b) Raw $\Delta\eta$ Balance Function

Figure 4.19: Raw Balance Functions for $(\Xi^- K^+ K^+)$

To obtain our final result, we mix events according to the method explained in section 3.3.4 to get rid of kaon pair correlations. We observe in figure 4.20a that the range of the correlation function for the $\Delta\phi$ distribution is smaller and does not match the range of the same event balance function in figure 4.19a. The same can be said or the $\Delta\eta$ distribution, the ranges are different for 4.20b and 4.19b. This alters our final results in figure 4.21, where we can still observe two negative peaks at $\Delta\phi(\Xi^- K_1^+) = \Delta\phi(\Xi^- K_2^+) = 0$ and $\Delta\phi(\Xi^- K_1^+) = \Delta\phi(\Xi^- K_2^+) = \pi$. The $\Delta\eta$ BF seems on the other hand rather flat. As observed in section 4.1.3, the $(\Xi^- K^+ K^+)$ BF is significantly smaller than the two-particle $(\Xi^- K^+)$ correlations from figure 4.13a.

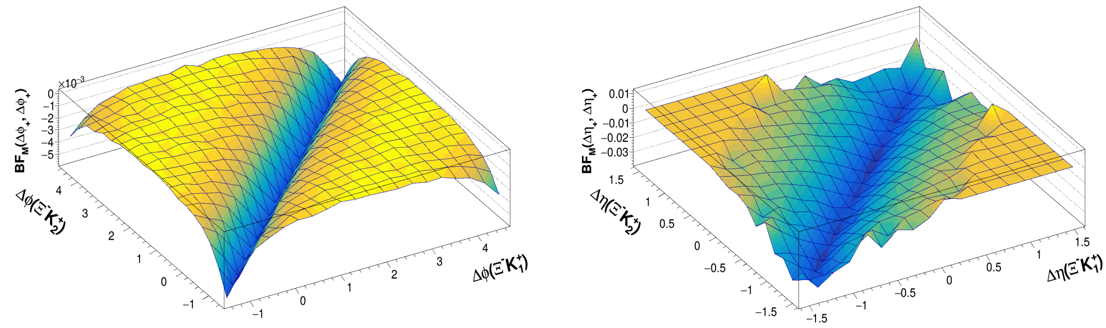

(a) Mixed Events $\Delta\phi$ Balance Function (b) Mixed events $\Delta\eta$ Balance Function

Figure 4.20: Mixed Events Balance Functions for $(\Xi^- K^+ K^+)$

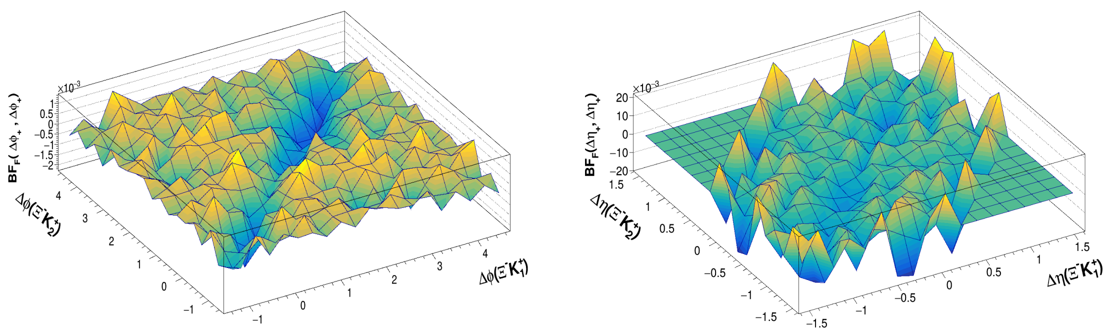

(a) Final $\Delta\phi$ Balance Functions for $(\Xi^- K^+ K^+)$ (b) Final $\Delta\eta$ Balance Functions for $(\Xi^- K^+ K^+)$

Figure 4.21: Final Balance Functions for $(\Xi^- K^+ K^+)$

The difference between the real data results and the MC results appears to come from mixed events correlations, similarly to our conclusion regarding the results between the MC BFs and the biased simulation results. As another quality assurance plot and similarly to what we did previously with the MC samples, we also plotted the BF for $\Delta\phi$ and $\Delta\eta$ for different ranges of the multiplicity. The results are shown in figures 4.22 and 4.23. As stated in section 3.3.5, the multiplicity is in percentile, and a low percentile stands for a high multiplicity.

For the multiplicity dependent BF for $\Delta\phi$ presented in figure 4.22, we observe one negative peak around $\Delta\phi(\Xi^- K_1^+) = \Delta\phi(\Xi^- K_2^+) = \pi$ for low multiplicity percentile (hence high multiplicity), but the ridge behaviours seems to have disappeared. For higher multiplicity percentile (hence lower multiplicity), the ridge becomes more apparent, with more negative values towards $(\Delta\phi,\Delta\phi) = 0$. However the small size of the Balance Function makes it difficult to differentiate between the BF shape and the fluctuations. For the multiplicity dependent BF for $\Delta\eta$ presented in figure 4.23, the low multiplicity percentile (or high multiplicity) BF show a peak at $\Delta\eta(\Xi^- K_1^+) = \Delta\eta(\Xi^- K_2^+) = 0$, which is the expected behaviour according to figure 4.12b. For lower multiplicities, the ridge behaviour is visible, with even a negative peak at $(\Delta\eta,\Delta\eta) = 0$ for a multiplicity between 40 and 60%. The multiplicity-dependent study clearly illustrates the challenge of obtaining a precise description of the "random trigger" component using mixed events, particularly in collisions with few produced particles.

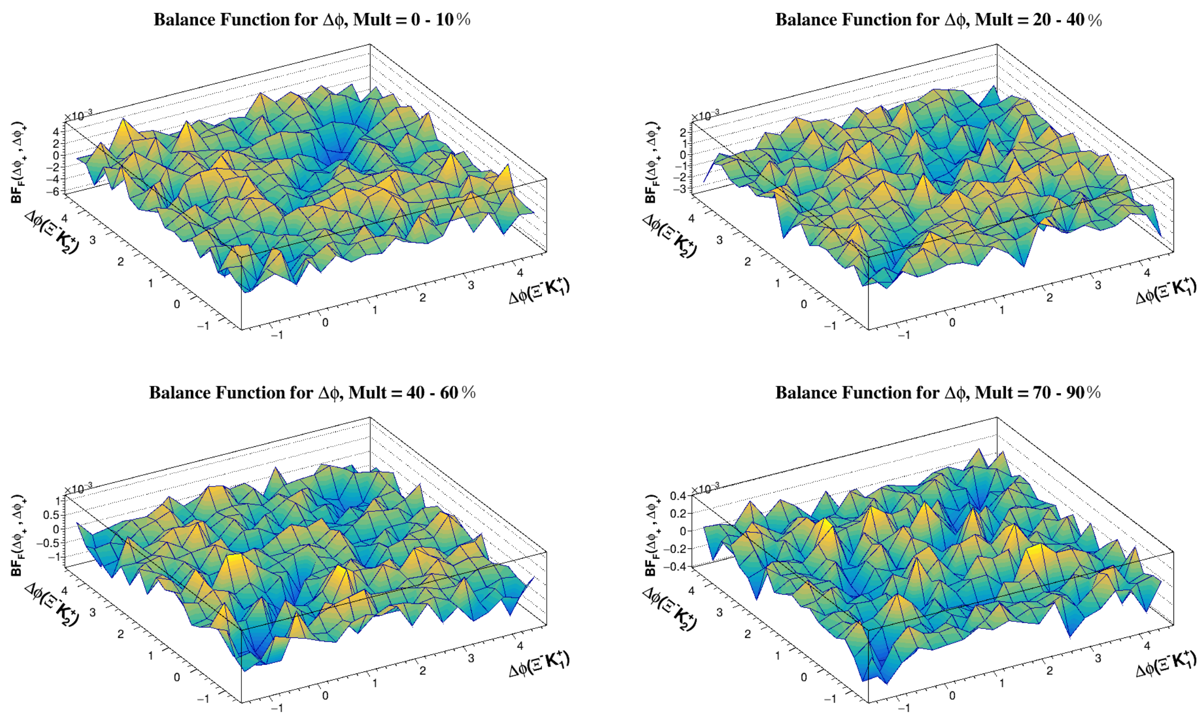

Figure 4.22: Corrected Balance Functions for $\Delta\phi$ different ranges of multiplicity

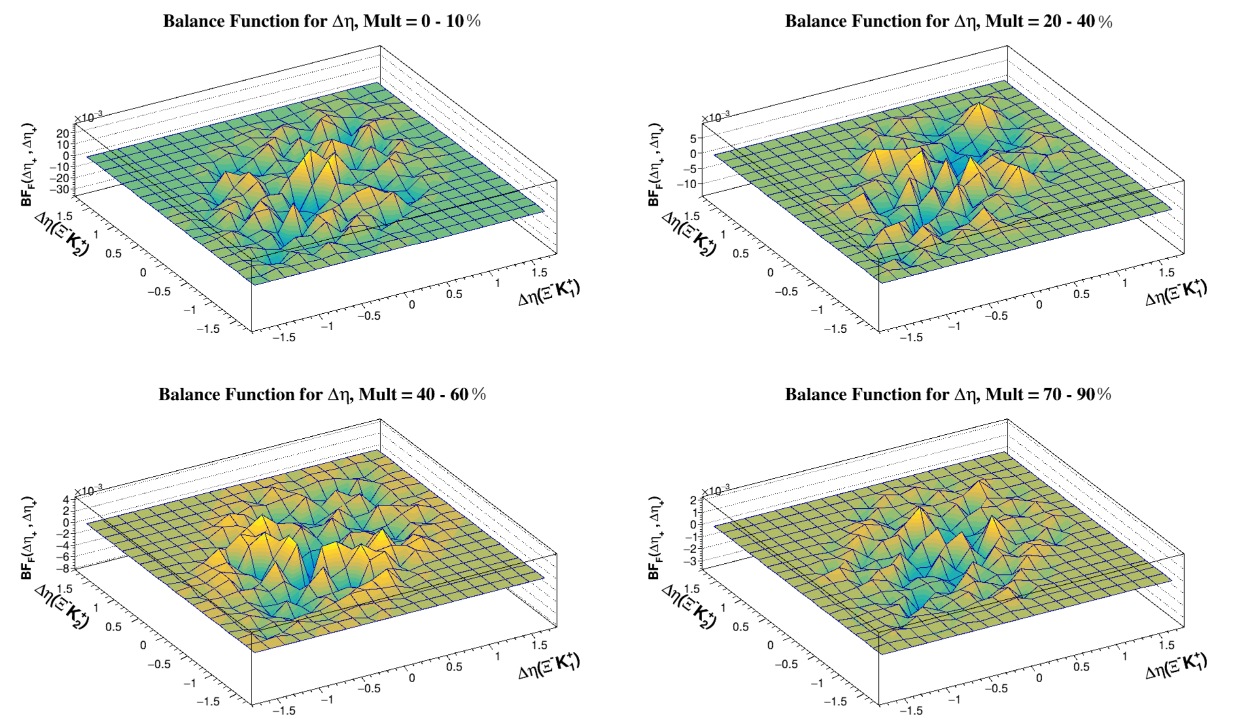

Figure 4.23: Corrected Balance Functions for $\Delta\eta$ different ranges of multiplicity

5 Conclusion

The aim of the study performed in this thesis was to compare the angular correlations in $\Delta\phi$ and $\Delta\eta$ for the $(\Xi^- K^+ K^+)$ triplet between Monte-Carlo simulated data and real data from the ALICE detector, in order to have a better understanding of strangeness balancing.

Through every analysis step, we have observed that production mechanisms were similar between the MC and the real data. The observation was the same for the final Balance Functions: the mixed event corrections we implemented to remove the uncorrelated triggers are not sufficient, and some two-particle correlation effects are still present in our final result after correcting for the uncorrelated triggers in the Balance Function. The results from our MC analysis and the real data analysis underline the challenge of event mixing when approaching three particle correlations, expanding on this part of the analysis would then help us improve our final result. The study of Balance Functions with respect to multiplicity however allowed us to observe, simultaneously with the multiplicity dependency, some angular positions that seem to be favoured for the triplet production, as the negative peaks at $\Delta\phi(\Xi^- K_1^+) = \Delta\phi(\Xi^- K_2^+) = 0$ and $\Delta\phi(\Xi^- K_1^+) = \Delta\phi(\Xi^- K_2^+) = \pi$ might suggest. The needed mixed event corrections prevent us from drawing conclusions on the nature of those peaks, but their presence is confirmed, whether are they positive and represent a favoured position in the azimuthal angle space, or negative and represent a disfavoured position.

A verification on the results of our analysis has been to perform a biased simulation, where we observed that for a perfectly balanced string with the strangeness only existing and being balanced by this $(\Xi^- K_1^+ K_2^+)$ triplet, the particles are produced close to each other in the azimuthal angle space, at $\Delta\phi(\Xi^- K_1^+) = \Delta\phi(\Xi^- K_2^+) = 0$. A very small amount of those triplets is also produced back-to-back at $\Delta\phi(\Xi^- K_1^+) = \Delta\phi(\Xi^- K_2^+) = \pi$, but almost insignificantly compared to the nearby production. The same analysis for $\Delta\eta$ showed that the particles in the triplet are produced close to each other in pseudorapidity, with a clear peak at $\Delta\eta(\Xi^- K_1^+) = \Delta\eta(\Xi^- K_2^+) = 0$. Another comparison on the MC data could be to alter the bias on strange particles, allowing the formation of other strange mesons or baryons in order to compute the balance function instead of the correlation function and observe how does the result change.

The next step of our analysis would be to try to understand this difference regarding this optimal simulation and the results we obtained while taking into account a normal particle event production. Moreover, the tracking efficiency correction for the kaons has not been taken into account in our results. We do not expect it to change the shape of the correlations, but it would provide us with more precise sizes for the correlation functions and the balance functions. Finally, a focused analysis on the systematic uncertainties should improve our final results.

Despite the number of corrections needed to have a definitive result on how strangeness is balanced in the $(\Xi^- K^+ K^+)$ triplet, our analysis shows through the size of the Balance Functions that the Ξ^- baryon does not tend to be balanced by two strange mesons. This motivates a future analysis on the angular correlations for a triplet balancing the baryon number itself, such as $(\Xi^- \bar{\Lambda} K^+)$, to study if the signal is more significant, hence favoured for strangeness balancing.

References

[1] **ALICE** Collaboration, J. Adam *et al.*, "Enhanced production of multi-strange hadrons in high-multiplicity proton-proton collisions", *Nature Phys.* **13** (2017) 535–539, arXiv:1606.07424 [nucl-ex].

[2] C. Bierlich *et al.*, "A comprehensive guide to the physics and usage of PYTHIA 8.3", *SciPost Phys. Codeb.* **2022** (2022) 8, arXiv:2203.11601 [hep-ph].

[3] J. Adolfsson *et al.*, "QCD challenges from pp to A–A collisions", *Eur. Phys. J. A* **56** (2020) 288, arXiv:2003.10997 [hep-ph].

[4] G. Barr, R. Devenish, R. Walczak, and T. Weidberg, *Particle Physics in the LHC era*. Oxford master series in particle physics, astrophysics and cosmology. Oxford University Press, Oxford, 2016.

[5] Wikimedia Commons, "Standard model of elementary particles." https://upload.wikimedia.org/wikipedia/commons/0/00/Standard_Model_of_Elementary_Particles.svg. Accessed May 2026.

[6] **Particle Data Group** Collaboration, S. Navas *et al.*, "Review of particle physics", *Phys. Rev. D* **110** (2024) 030001.

[7] J. Rafelski, "Strangeness Production in the Quark Gluon Plasma", *Nucl. Phys. A* **418** (1984) 215C–235C.

[8] **ALICE** Collaboration, S. Acharya *et al.*, "The ALICE experiment: a journey through QCD", *Eur. Phys. J. C* **84** (2024) 813, arXiv:2211.04384 [nucl-ex].

[9] **ALICE** Collaboration, B. B. Abelev *et al.*, "Multi-strange baryon production at mid-rapidity in Pb-Pb collisions at $\sqrt{s_{NN}} = 2.76$ TeV", *Phys. Lett. B* **728** (2014) 216–227, arXiv:1307.5543 [nucl-ex]. [Erratum: Phys.Lett.B 734, 409–410 (2014)].

[10] **ALICE** Collaboration, K. Aamodt *et al.*, "The ALICE experiment at the CERN LHC", *JINST* **3** (2008) S08002.

[11] O. Matonoha, *Production of strangeness in partonic interactions at the LHC*. PhD thesis, 2023-05-22, Lund University, Lund U., 5, 2023.

[12] M. Brice, "Aerial view of the CERN accelerator complex." https://cds.cern.ch/record/1295244, 2008. Accessed May 2026.

[13] A. Tauro, "3D ALICE Schematics of ALICE during RUN2 and after the upgrade, for RUN3." https://cds.cern.ch/record/2263642?ln=en, 2017. Accessed May 2026.

[14] CERN, "The L3 experiment." https://home.cern/science/experiments/l3/. Accessed May 2026.

[15] **ALICE** Collaboration, B. B. Abelev *et al.*, "Performance of the ALICE Experiment at the CERN LHC", *Int. J. Mod. Phys. A* **29** (2014) 1430044, arXiv:1402.4476 [nucl-ex].

[16] **ALICE** Collaboration, H. S. Scheid, "Future ALICE Upgrades for Run 4 and Beyond", *Acta Phys. Polon. Supp.* **16** (2023) 1–A145, arXiv:2211.04802 [nucl-ex].

[17] **ALICE** Collaboration, G. Dellacasa *et al.*, "ALICE: Technical design report of the time projection chamber", Tech. Rep. CERN-OPEN-2000-183, CERN-LHCC-2000-001, 1, 2000.

[18] **ALICE** Collaboration, G. Dellacasa *et al.*, "ALICE technical design report of the time-of-flight system (TOF)", Tech. Rep. CERN-LHCC-2000-012, 2, 2000.

[19] **ALICE** Collaboration, S. Acharya *et al.*, "J/ψ production at midrapidity in p$-$Pb collisions at $\sqrt{s_{\mathrm{NN}}} = 8.16$ TeV", *JHEP* **07** (2023) 137, arXiv:2211.14153 [nucl-ex].

[20] ALICE Collaboration, "A *pp* collision at 13 TeV seen by ALICE during the start of RUN2 in 2016." https://cds.cern.ch/record/2149032, 2016. Accessed May 2026.

[21] J. Allen *et al.*, "ALICE DCal: An Addendum to the EMCal Technical Design Report Di-Jet and Hadron-Jet correlation measurements in ALICE", Tech. Rep. CERN-LHCC-2010-011, ALICE-TDR-14-add-1, 5, 2010.

[22] V. Kučera, *Study of strange particle production in jets with the ALICE experiment at the LHC*. PhD thesis, Charles U., Prague (main), 2016.

[23] CERN, “LHC report: Make way for the heavy ions.” https://home.cern/news/news/accelerators/lhc-report-make-way-heavy-ions, March, 2023. Accessed May 2026.

[24] L. Lönnblad and H. Shah, “Baryon correlations in Pythia”, *Eur. Phys. J. C* **83** (2023) 1105, arXiv:2309.01557 [hep-ph].

[25] R. Brun and F. Rademakers, “ROOT: An object oriented data analysis framework”, *Nucl. Instrum. Meth. A* **389** (1997) 81–86.

[26] A. Chu, Y. Liu, and M. Needham, “Improving systematic uncertainties on precision two-body mass measurements”, *EPJ Tech. Instrum.* **13** (2026) 3, arXiv:2509.26130 [hep-ex].

[27] **ALICE** Collaboration, S. Acharya *et al.*, “Studying strangeness and baryon production mechanisms through angular correlations between charged Ξ baryons and identified hadrons in pp collisions at $\sqrt{s} = 13$ TeV”, *JHEP* **09** (2024) 102, arXiv:2308.16706 [hep-ex].

[28] J. L. Nagle and W. A. Zajc, “Small System Collectivity in Relativistic Hadronic and Nuclear Collisions”, *Ann. Rev. Nucl. Part. Sci.* **68** (2018) 211–235, arXiv:1801.03477 [nucl-ex].

[29] J. Adolfsson, *Study of Ξ-Hadron Correlations in pp Collisions at $\sqrt{s} = 13$ TeV Using the ALICE Detector*. PhD thesis, Lund U., 2020.

[30] ROOT Team, *ROOT Manual: TH2D Class Reference*. CERN, 2024. Accessed May 2026.

[31] K. Haupt, “Probing charm production with three-particle correlations in pp collisions”, Master’s thesis, Lund U., 2023.

Appendix

A. Additional tables and figures

Detector acceptance corrections

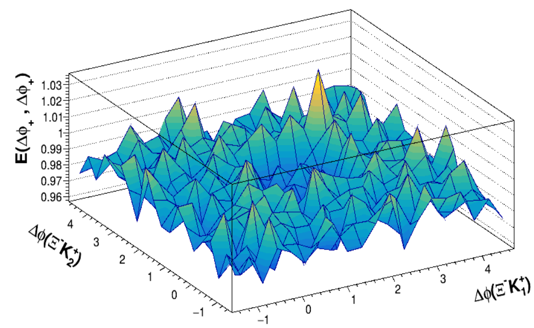

(a) $\Delta\phi$ $\Xi^- K^+ K^+$

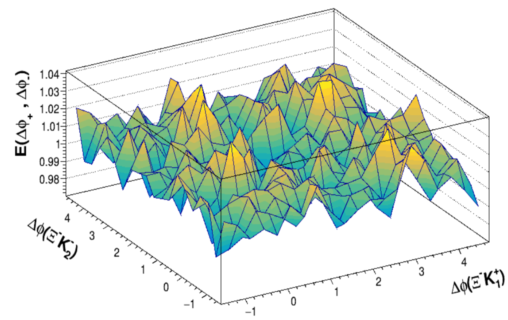

(b) $\Delta\phi$ $\Xi^- K^+ K^-$

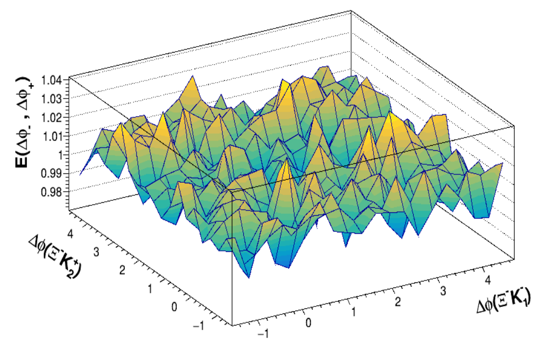

(c) $\Delta\phi$ $\Xi^- K^- K^+$

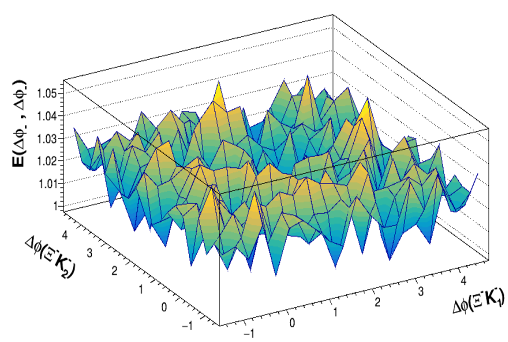

(d) $\Delta\phi$ $\Xi^- K^- K^-$

Figure A1: Detector Acceptance Corrections for MC for $\Delta\phi$

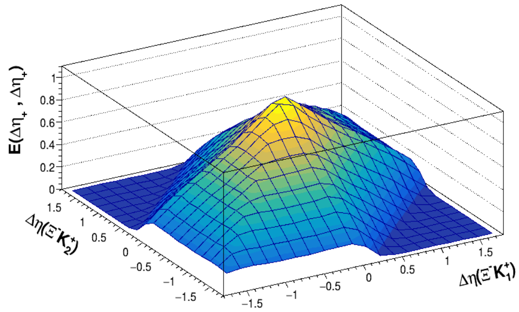

(a) $\Delta\eta\ \Xi^- K^+ K^+$

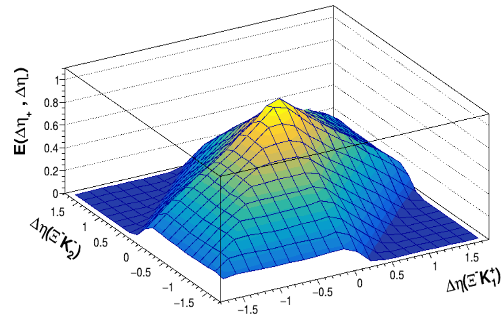

(b) $\Delta\eta\ \Xi^- K^+ K^-$

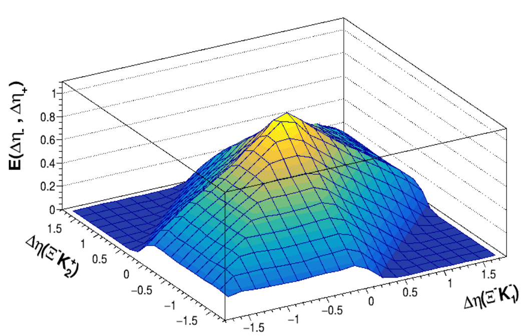

(c) $\Delta\eta\ \Xi^- K^- K^+$

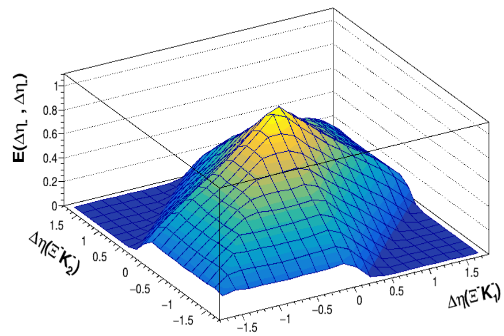

(d) $\Delta\eta\ \Xi^- K^- K^-$

Figure A2: Detector Acceptance Corrections for MC for $\Delta\eta$

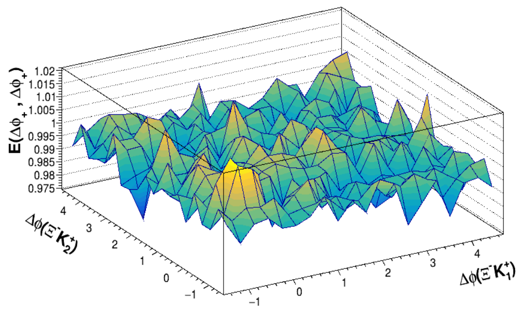

(a) $\Delta\phi$ $\Xi^{-}K^{+}K^{+}$

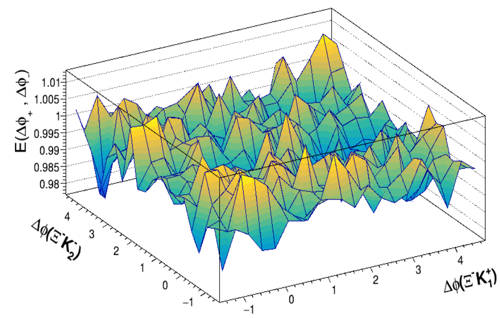

(b) $\Delta\phi$ $\Xi^{-}K^{+}K^{-}$

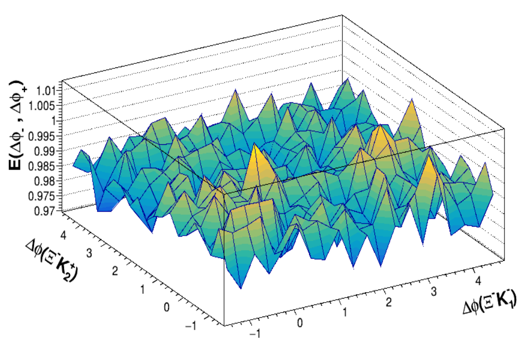

(c) $\Delta\phi$ $\Xi^{-}K^{-}K^{+}$

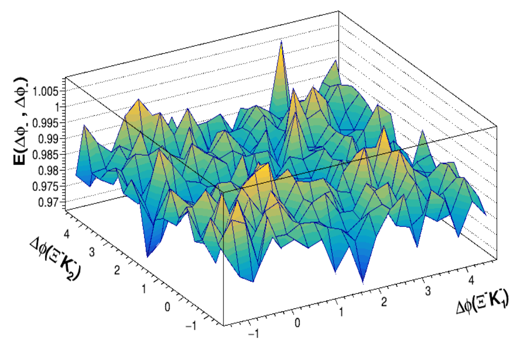

(d) $\Delta\phi$ $\Xi^{-}K^{-}K^{-}$

Figure A3: Detector Acceptance Corrections for real data for $\Delta\phi$

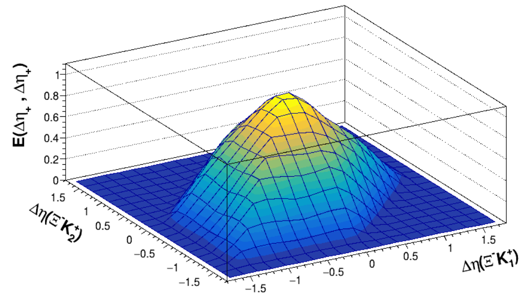

(a) $\Delta\eta$ $\Xi^- K^+ K^+$

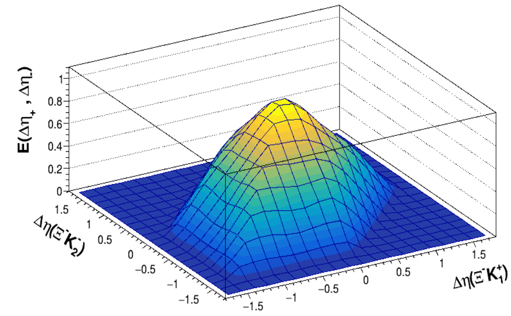

(b) $\Delta\eta$ $\Xi^- K^+ K^-$

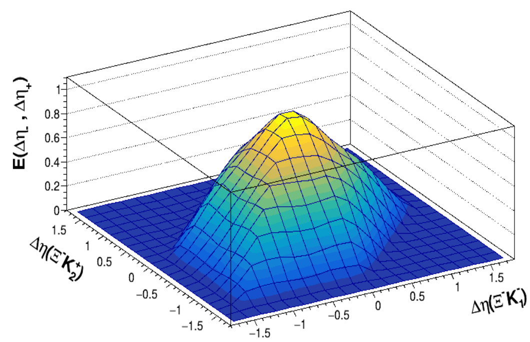

(c) $\Delta\eta$ $\Xi^- K^- K^+$

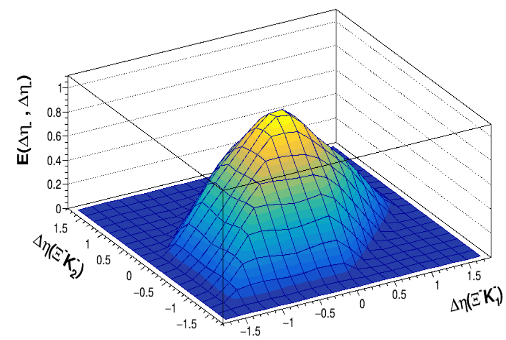

(d) $\Delta\eta$ $\Xi^- K^- K^-$

Figure A4: Detector Acceptance Corrections for real data for $\Delta\eta$

Fake Ξ^- candidates correlations

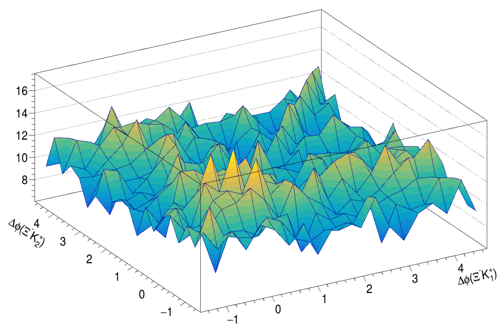

(a) Fake left-side $\Delta\phi(\Xi^- K^+ K^+)$

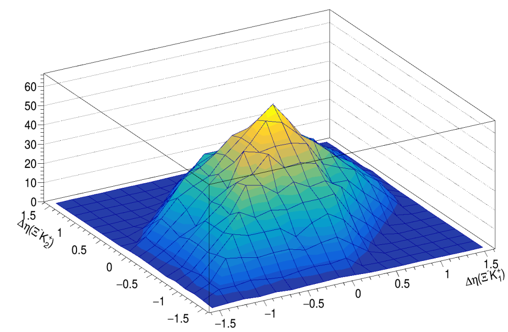

(b) Fake left-side $\Delta\eta(\Xi^- K^+ K^+)$

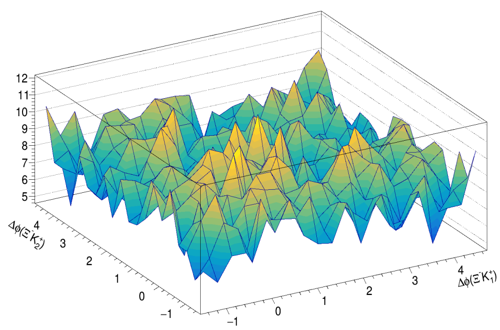

(c) Fake right-side $\Delta\phi(\Xi^- K^+ K^+)$

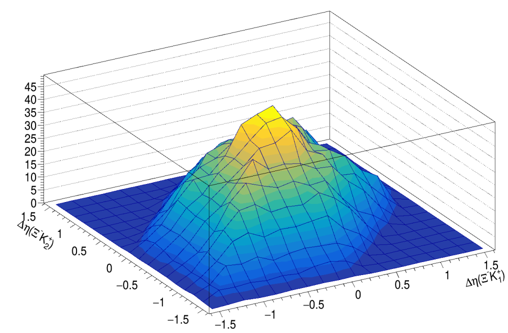

(d) Fake right-side $\Delta\eta(\Xi^- K^+ K^+)$

Figure A5: Correlations for fake Ξ^- candidates (the distributions are neither normalised nor corrected for detector acceptance). The left and right-side correspond respectfully to the left and right-side of the peak region, as presented in figure 3.1.